TECHNISCHE UNIVERSITÄT WIEN
Vienna University of Technology

MASTERARBEIT

Accounting for the Role of Trees in Urban Energy Balance Modeling Using GIS Techniques

ausgeführt zum Zwecke der Erlangung des akademischen Grades eines Diplom-Ingenieur

unter der Leitung von
Univ. Prof. Dipl.-Ing. Dr. techn. Ardeshir Mahdavi
E 259/3 Abteilung für Bauphysik und Bauökologie
Institut für Architekturwissenschaften

eingereicht an der
Technischen Universität Wien
Fakultät für Architektur und Raumplanung

von

Kristopher Hammerberg

Matrikelnr. 1126359
Gerhardusgasse 9/21, 1200 Wien

Wien, im Jänner 2014

Abstract

This thesis work addresses the effect of trees on the urban energy balance and examines two methods for accounting for their impact in micro-climate modeling. The primary objective was to explore the ways that trees influence the exchange of radiation within the urban environment, namely the obstruction of the sky to nocturnal long-wave radiative cooling and the interception of direct short-wave solar radiation.

In pursuit of this goal, this study employed computational methods involving high resolution digital models of the city of Vienna, Austria. They were used to calculate continuous sky view factor (SVF) maps and estimate global solar radiation in urban street canyons. Both methods were compared to on-site measurements for validation.

Additionally, the strength of the relationship between SVF and urban heat island intensity (UHII) was also explored. In order to achieve this, 5 urban study areas and one rural reference area were selected. Each study area was centered around a longterm weather station. In each area it was necessary to distill a single area mean value of SVF from the continuous SVF maps to compare against the UHII value. Several methods for area mean sampling were compared in view of the strength of their relationship to UHII.

Acknowledgments

Foremost, I must thank my parents for instilling within me a deep love of learning and that sense of wonder and curiosity with the world, which is the engine of scientific inquiry. Without their support and encouragement throughout my academic career this would not be possible.

Without the guidance, motivation, and advice of my supervisor, Professor Dr. Ardeshir Mahdavi, I'd still be adrift upon the sea of my own mind. Additionally, this work has been influenced and aided by many of my colleagues at the Department of Building Physics and Building Ecology. Many thanks to Josef Lechleitner, Milena Vuckovic, Aida Maleki, Kristina Kiesel, and the UHI team. I'd also like to thank Rukiye Cetin for the generous contribution of data from her solar irradiance measurements.

Above all, my wife Betsy deserves more than these simple words of gratitude for her constant support and encouragement. Her love is the light by which I set my course and the sustenance that has seen me through.

Table of Contents

1 Introduction

1.1 Overview

This research investigates methods of quantifying the effect of trees on the radiation exchange in urban environments using geospatial information system (GIS) software and commonly available municipal data. This research was undertaken as part of the ongoing Urban Heat Island Project. That project is aimed at “developing mitigation and risk prevention and management strategies concerning the urban heat island (UHI) phenomenon” (UHI 2013).

The work is divided into two avenues of research: the characterization of longwave radiation exchange with sky view factors and the calculation of the incoming shortwave radiation in the urban environment. The methodological approach of this research combines the implementation of analytical models with empirical field measurements.

1.2 Motivation

The influences on the urban microclimate are many and varied. They include both spatially dynamic factors such as building geometry, vegetation, and material properties, as well as temporally dynamic factors such as wind speed, solar radiation, and anthropogenic heat output (Oke 1987). For instance, compared to a rural environment, urban buildings provide more surface area of materials that absorb and store more solar radiation (Gartland 2011), while at the same time reducing the amount of visible sky available for nocturnal cooling (Oke 1981). Taken together, these factors tend to increase the temperature of an urban area as compared to its rural surroundings. This phenomenon is commonly referred to as the Urban Heat Island (Voogt 2002) and is characterized by the term Urban Heat Island Intensity (UHII or $\Delta\theta$), which is the difference between urban and rural air temperatures (see fig. 1).

In the United Nations' Department of Economic and Social Affairs, Population Division's biennial report on the projections of urban and rural populations (2012), they estimate that the global population living in urban areas will increase by 72 percent, from 3.6 billion in 2011 to 6.3 billion in 2050. In other words, by 2050 the global urban population will be nearly equal to the entire world’s total population in 2002. Combined with increasing average temperatures due to climate change, the UHI effect will have an ever larger impact on a growing number of people. These impacts will include adverse health effects, such as increased rates of “heat-related illness”

(Harlan et al. 2011), and increased energy demand due to a higher use of air conditioning (Akbari 2005).

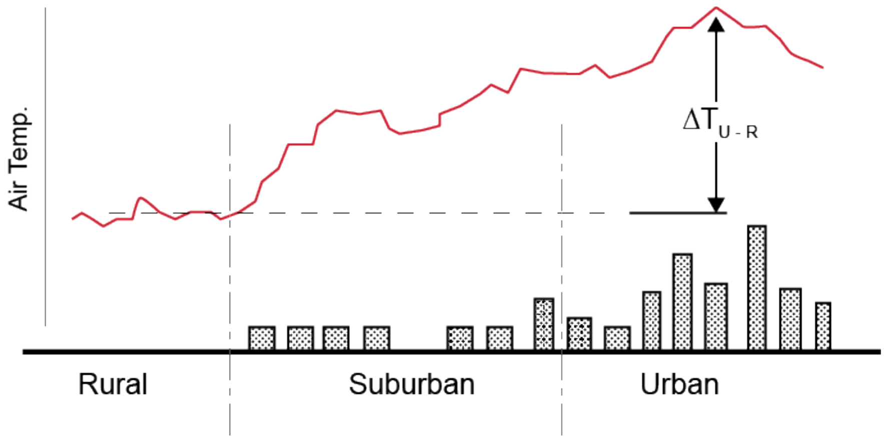

Figure 1. *Idealized cross section of a typical urban heat island. Adapted from (Oke 1987) with permission.*

Planting trees is a frequently proposed mitigation strategy for reducing UHII. A simple approach to quantifying their impact using readily available municipal geospatial information and weather station measurements could serve as a useful decision-support tool for studying site specific impacts.

Additionally, better models of the radiation exchange in urban environments will lead to increased accuracy in building performance simulation for urban structures. Radiation exchange has a significant impact on surface temperatures and thus transfer by conduction. This contributes significantly to a building's energy budget and, by extension, the energy budget of the entire urban environment (Robinson 2011).

1.3 Structure

To frame this work in the current context, section 2 covers the relevant background literature and discusses several parallel efforts of modelling the radiative exchange in urban environments.

The methodology is presented in section 3. It begins with a description of the input data sources. Then the implementation of an algorithm to calculate SVF maps is discussed, as well as the various area mean sampling methods and the measurement techniques used for validation. This is followed by an explanation of how this algorithm was adapted to estimate global irradiance values and the on-site verification measurements.

Section 4 contains the results of the research and it is followed by the discussion and conclusions in Sections 5 and 6, respectively.

2 Background

2.1 Existing Models

Several models have been developed that include the effect of trees on the urban environment. They are discussed below to highlight the broad range of current approaches and identify similarities. At one end of the spectrum is ENVI-met, a sophisticated three-dimensional, first-principles model of the “surface-plant-air interactions” in the urban micro-climate (Bruse 2004). This software can be used to simulate a small urban area over a short time period and it requires detailed and specialized input, including the manual creation of a software specific model. The radiative transfer component of this model has been shown to correspond well with measured values (Samaali, et al. 2007). In addition to radiative transfer, the model accounts for many of the other effects of vegetation, such as their effect on wind-speed and evapotranspiration (Bruse 2004).

At the other end of the spectrum is i-Tree (formerly UFORE), a suite of tools that relies on statistical extrapolation from extensive tree inventories or limited web-based user input to estimate the annual benefits in terms of monetary value (USDA Forest Service 2012). While it is certainly capable of helping urban planners and policy-makers with general value-based decisions, it lacks a physical representation of urban geometry necessary for site specific inquiries or micro-climate predictions.

RayMan is a software model with a focus on simulating longwave and shortwave radiation flux in order to calculate mean radiant temperature in urban areas. This can then be used with thermal sensation indices like Predicted Mean Vote (Matzarakis, et al. 2010). RayMan relies on a fully 3D vector model of the urban environment. In terms of modelling accuracy, this is an advantage over 2.5D raster models, such as the one used in this study. However, as of this writing, it requires the manual creation of the geometric model within the software itself, without the ability to import from well-known computer-aided design (CAD) files.

The Green CTTC (cluster thermal time constant) model is a general analytical model for estimating the air temperature in the urban canopy layer (Shashua-Bar and Hoffman 2002). It is a relatively simple parameterized model that uses derived geometric properties of the environment rather than a complete geometric model. Thus within the “cluster” in question, there is no consideration of spatial distributions.

In view of creating a model which could be used by city planning professionals with existing data sources, this research effort is based on a simplification of the SOLWIEG model developed by the

Department of Earth Sciences at the University of Göteborg. This model simulates both longwave and shortwave radiation flux, as well as mean radiant temperature. For input, it requires measured values of global radiation, air temperature, relative humidity. Additionally, the urban geometry and tree canopy is represented with high-resolution digital elevation models (DEM) (Lindberg, et al. 2008).

2.2 Radiative Modeling in Urban Environment

Shortwave radiation from the sun is absorbed by the surfaces in an urban area in the range of 0.3μm to 3μm. Radiative heat transfer, or longwave radiation exchange, between these surfaces occurs in the spectrum 3-4μm to 100μm. This leads to a “two-hand model for radiation exchange” (Robinson 2011).

Robinson also notes that compared to rural or unobstructed sites, simulating radiation balance in the urban context is made more complex by the surrounding built surfaces. For instance, radiation reflected from these surfaces deeper into the urban canyon is likely to be reabsorbed by another surface (see fig. 2). This is often referred to as “radiation trapping” and Oke (1987) characterizes this with lower than average albedo values for urban areas. Furthermore these relatively warm surroundings obstruct the cooler night sky and influence the longwave radiation balance (Oke).

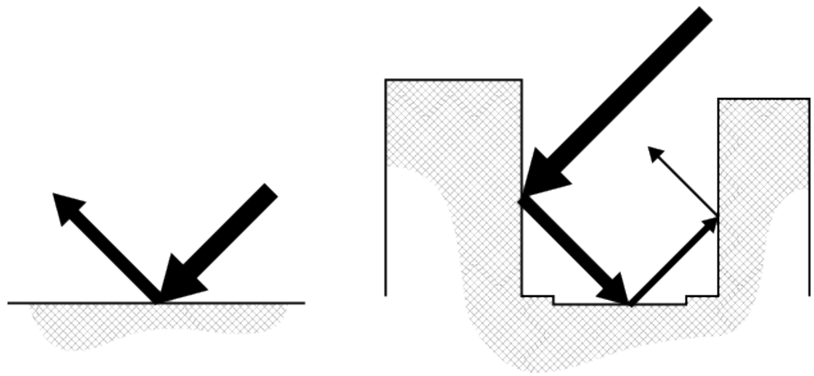

Figure 2. *Reflection in an unobstructed environment (left) compared to radiation trapping in typical urban canyon (right).*

2.2.1. Longwave Radiation and Sky View Factor

Longwave radiation exchange from the earth to the cool night sky is the primary forcing mechanism of nocturnal cooling (Unger 2009) and on calm, clear nights it is the dominate factor influencing air temperature changes (Nunez and Oke 1976).

The net longwave radiation between a surface and its environment, in its most basic representation, is given by a simple application of the Stefan-Boltzmann law for the radiant exitance of a grey body,

$$\Phi = \varepsilon \sigma T^4 \quad (1)$$

such that

$$I_L = \varepsilon \sigma \left(T_{env}^4 - T_s^4 \right) \quad (2)$$

where σ is the Stefan-Boltzmann constant, ε is the thermal emissivity, T_{env} is the surface temperature for the surroundings (in degrees Kelvin), and T_s is the external temperature of the surface (Robinson 2011).

Surrounding buildings reduce the amount of sky available for radiation exchange, replacing it with relatively warmer surfaces. The extent to which the sky is obstructed is called the sky view factor (SVF) and is discussed in more detail below.

2.2.1.1. Sky View Factor

SVF is defined as the fraction of radiant flux from a surface point that reaches the sky hemisphere (Johnson and Watson 1984). It is a measure for the openness of the sky to radiation exchange given surrounding obstructions. SVF ranges from 0 to 1, where 0 is a completely enclosed area with no direct view to the sky and a value of 1 indicates a complete open area with no obstructions.

Following figure 3, SVF can be expressed as

$$\Psi = \frac{1}{\pi R^2} \int_{S_v} \cos(\phi) \, dS \quad (3)$$

where S_v is the visible portion of a sky hemisphere of radius R. In this representation, the visible sky is the portion not obscured by the projection of the obstructing surface on the sky hemisphere (see fig. 4)

Using this definition of SVF and equation (1), longwave radiation flux from the sky is

$$I_L^{\downarrow} = \Psi \varepsilon \sigma T^4 \quad (4)$$

where ε and T are the emissivity and the temperature of the sky, respectively.

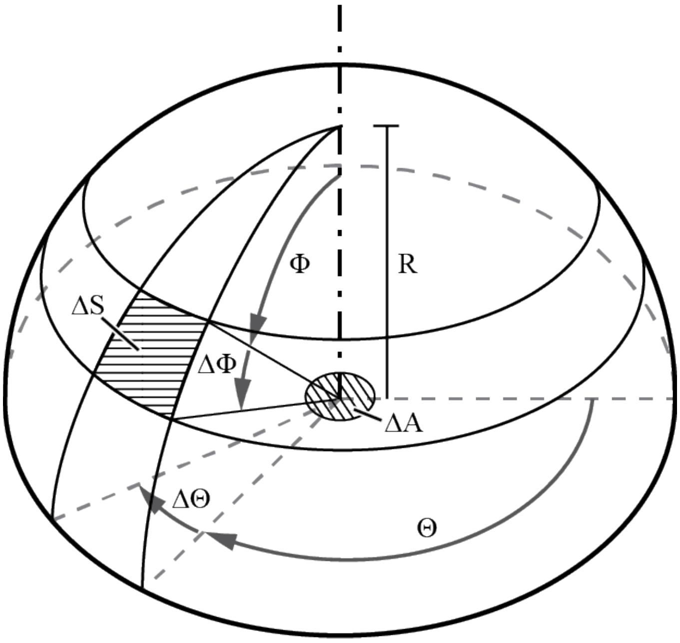

Figure 3. *Radiant exchange between sky and surface. Adapted from (Johnson & Watson, 1984) (c) American Meteorological Society. Used with permission.*

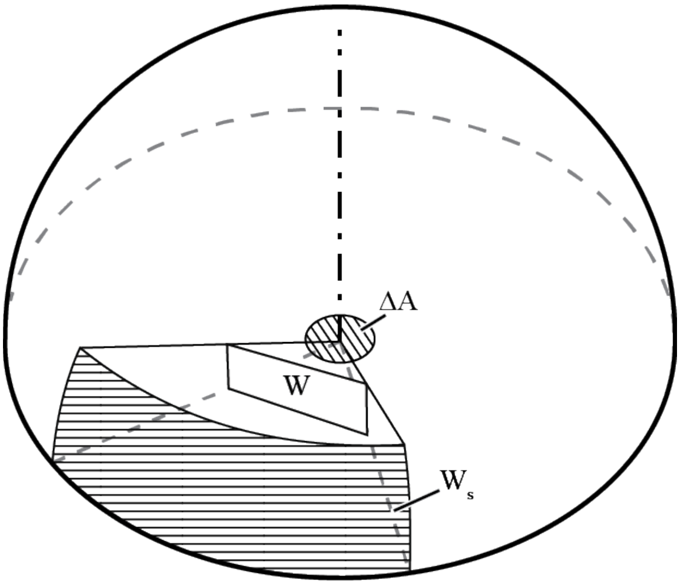

Figure 4. *Projection (W_s) of a wall obstruction (W) on to the sky hemisphere. Adapted from (Johnson & Watson, 1984) (c) American Meteorological Society. Used with permission.*

SVF is a common parameter in models calculating longwave radiation. In the absence of a tree canopy, the SOLWEIG model expresses incoming longwave radiation as a combination of three terms: direct longwave radiation from the sky, wall radiation, and reflected radiation from the sky. Each term uses equation (1) modified by the SVF or one minus the SVF to account for its portion of radiative exchange, giving

$$I_L^{\downarrow} = \Psi \varepsilon_{sky} \sigma T_a^4 + (1-\Psi) \varepsilon_w \sigma T_s^4 + (1-\Psi)(1-\varepsilon_w) \varepsilon_{sky} \sigma T_a^4 \tag{5}$$

where Ψ is the SVF, T_a is the air temperature, T_s is the surface temperature, ε_{sky} and ε_w are the thermal emissivity of the sky and surrounding walls, respectively (Lindberg, et al. 2008).

As an example of how SVF can be used to estimate the impact of longwave radiation on air temperature, the Green CTTC model uses the following formula

$$\Delta T_{NLWR} = \frac{(\sigma \varepsilon T_s^4 - \sigma B_r T_a^4) \Psi}{h} \tag{6}$$

where ε is the thermal emissivity of the ground, B_r is the effective emissivity of the atmosphere parametrized by vapor pressure, T_a and T_s are the temperatures of the air and surface temperatures, respectively. Ψ is the representative sky view factor of the area. The denominator, h, is the heat transfer coefficient at the surface (Shashua-Bar and Hoffman 2002).

During the course of this research it was not possible to test these models with direct measurements of the longwave radiation exchange or surface temperature. However, in other studies SVF has shown strong correlation with downward radiative flux (Nunez et al. 2000, Blankenstein and Kuttler 2004). For the purposes of this study, SVF will serve as a proxy variable for longwave radiation flux. Considering only SVF does not account for the emissivity or temperature of the sky or urban surfaces. However, it can be considered the primary contribution of urban morphology to the longwave radiation balance.

2.2.2. Shortwave Irradiance

As solar radiation passes through the atmosphere a portion of it is reflected and absorbed by atmospheric particles and molecules. The part that is reflected (scattered) in combination with the portion that is reflected from the earth to the atmosphere and back again (back-scattered), is called the diffuse component. The part that is transmitted directly without interference is called the direct component (Oke 1987). Together they constitute the global shortwave radiation.

In order to reduce modeling complexity, the diffuse component is often assumed to be received in equal proportions from all parts of the sky hemisphere (i.e. an isotropic sky). In reality, this is not the case. Even during perfectly diffuse conditions the radiance of the sky increases towards the zenith. With a clear sky, the diffuse portion is higher near the sun (circumsolar brightening) and at the horizon as a result of back-scattering beyond the horizon (horizon brightening) (Robinson 2011). The models discussed below, as well as the one employed in this research, all assume an isotropic sky.

The direct solar irradiance incident on an unobstructed horizontal surface is

$$I_{dir}^{\downarrow,s} = I_{dir} \sin(h) \tag{7}$$

where I_{dir} is the direct normal irradiance (DNI) and h is the solar altitude angle.

The presence of an opaque obstruction that casts a shadow on the surface reduces the direct component to 0. However, the surface will still receive diffuse radiation corresponding to

$$I_{dif}^{\downarrow,s} = \Psi I_{dif} \tag{8}$$

where Ψ is the sky view factor and I_{dif} is the diffuse fraction measured at an unobstructed reference point.

Additionally, the shaded surface will also receive reflected shortwave radiation (both diffuse and direct) from the surrounding surfaces. This contribution is perhaps the most difficult to calculate. It is possible to employ a radiosity algorithm or a detailed Monte Carlo ray-tracing program such as RADIANCE, however these are computationally expensive and more difficult to implement.

A more straight forward, but less accurate, approximation is to assume that all surrounding surfaces are reflecting some portion of the global irradiance equally. (Lindberg 2007) gives this term as

$$I_{ref}^{\downarrow,s} = (1-\Psi) I_G \ \alpha \ \sin(h) \tag{9}$$

where I_G is the global irradiance, α is the average albedo of the surrounding surfaces. The altitude angle of the sun, h, is included to account for fraction of the wall surface that is “available for reflection” throughout the day (Lindberg).

In clear sky conditions, the direct component has a much higher contribution to global shortwave irradiance than the diffuse fraction. Combined with the binary effect of solid shading obstructions, this results in extreme discontinuities across the boundary between sun and shade.

2.3 The Effects of Trees

2.3.1. Shortwave

As trees are not monolithic obstructions, they allow some direct shortwave radiation through gaps in the canopy. Neither are they entirely opaque, thus a portion of the incident solar radiation that strikes the leaves is transmitted. Additionally, some is diffusely scattered by multiple reflections within the canopy itself. The overall effect is that shortwave radiation attenuates exponentially when passing through a tree canopy (Ong 2003) and can be expressed by the Beer-Lambert law,

$$\frac{I_S^{\downarrow,i}}{I_S^{\downarrow,0}} = \mathrm{e}^{-k\times LAI} \tag{10}$$

where $I_S^{\downarrow,i}$ is the amount of radiation that passes through the canopy, $I_S^{\downarrow,0}$ is the total incident shortwave radiation above the canopy, LAI is the leaf area index, and k is an extinction coefficient that is specific to both the site and the species of tree (Jonckheere, et al. 2004).

In other words, the left hand side of this equation gives the fraction of radiation that passes through the tree canopy or the effective transmissivity, τ. The shading fraction is then simply

$$f_s = 1-\tau \tag{11}$$

The SOLWEIG mode accounts for the effect of trees as follows. It uses one representative value for the vegetation shading factor of an entire area and calculates incident shortwave radiation at a point with the following equation,

$$\begin{aligned} I_S^{\downarrow} = I_{dir}[S_b-(1-S_v)f_s]\sin(h) \\ +I_{dif}[\Psi_b-(1-\Psi_v)f_s] \\ +I_G\alpha[1-(\Psi_b-(1-\Psi_v)f_s)] \\ \times(1-w_s) \end{aligned} \tag{12}$$

where the first term computes the direct irradiance with I_{dir} as the direct component measured at an unobstructed reference point, f_s is the shading fraction of the tree canopy, h is the solar altitude angle, S_b and S_v are binary values indicating the presence [0] or absence [1] of shading from buildings and vegetation, respectively.

The second term accounts for diffuse radiation, where I_{dif} is the diffuse fraction measured at a reference location, Ψ_b and Ψ_v are the sky view factors considering buildings and vegetation, respectively. The third term is a representation of the reflected radiation, where I_G is the sum of I_{dir} and I_{dif}, α is the average albedo of the surrounding surfaces, and w_s is the fraction of the wall shadowed (Lindberg and Grimmond 2011).

Rather than relying on a single value for the shading fraction, ENVI-met calculates this for each tree based on a species specific leaf leaf area density (LAD) profile. LAD is the leaf surface area per volume. LAI is obtained by the one dimensional vertical integration of LAD as follows

$$LAI(z, z+\Delta z) = \int_{z'}^{z'+\Delta z} LAD(z') \; dz' \tag{13}$$

After the determination of LAI, a reduction factor for diffuse radiation, $\xi^{\downarrow}_{sw.dif}$ is calculated using (10). In the case of direct solar radiation, a three-dimensional LAI is calculated with respect to the angle of incidence and a separate reduction factor, $\xi^{\downarrow}_{sw.dir}$ is derived. If the sun is obstructed by a solid object, $\xi^{\downarrow}_{sw.dir}$ is set to 0. Then, the shortwave radiation budget is described with the following three equations for direct, diffuse, and reflected components, respectively.

$$I^{\downarrow}_{dir} = \xi^{\downarrow}_{sw.dir} \; I^{\downarrow,0}_{dir} \tag{14}$$

$$I^{\downarrow}_{dif} = \xi^{\downarrow}_{sw.dif} \; \Psi \; I^{\downarrow,0}_{dif} \tag{15}$$

$$I^{\downarrow}_{ref} = (1-\Psi) \; I^{\downarrow,0}_{dir} \; \alpha \tag{16}$$

where $I^{\downarrow,0}_{dir}$ and $I^{\downarrow,0}_{dif}$ are the direct and diffuse components at the boundary layer, Ψ is the SVF, and α is the average albedo for walls within the model (Huttner 2012).

2.3.2. Longwave

Accounting for the effects of trees on the longwave exchange has been handled in a variety of ways in the existing models. For example, the Green CTTC model incorporates only a simple reduction of the SVF by a factor of (1 – PSA_{tree}), where PSA_{tree} is the percent of the studied area covered by the tree canopy (Shashua-Bar and Hoffman 2002).

In the SOLWIEG-model, equation (5) is modified as follows to account for trees

$$\begin{aligned} I_L^{\downarrow} = & (\Psi_b + \Psi_v - 1)\varepsilon_{sky}\sigma T_a^4 \\ & + (2 - \Psi_v - \Psi_{vb})\varepsilon_w \sigma T_a^4 \\ & + (\Psi_{vb} - \Psi_b)\varepsilon_w \sigma T_s^4 \\ & + (2 - \Psi_b - \Psi_v)(1 - \varepsilon_w)\varepsilon_{sky}\sigma T_a^4 \end{aligned} \tag{17}$$

where there are now three separate calculations of SVF: the sky obstructed by buildings, the sky obstructed by vegetation, and the sky obstructed by both buildings and vegetation (Ψ_b, Ψ_v, and Ψ_{vb} respectively). This effects all terms in equation (17) and the second term is added to account for the additional longwave radiation from the canopy itself.

ENVI-met calculates the upward and downward dwelling longwave radiation at each discretized 3D grid location including inside the tree canopy itself. To simplify the comparison, the equations below describe the only the downward flux as influenced by an overhead canopy

$$I_L^{\downarrow} = \xi_L^{\downarrow} I_{L0}^{\downarrow} + (1 - \xi_L^{\downarrow})\varepsilon_f \sigma T_f^4 + (1 - \Psi)\varepsilon_w \sigma T_w^4 \tag{18}$$

and

$$\xi_L^{\downarrow} = e^{-k \cdot LAI} \tag{19}$$

where the first term is the total incoming longwave radiation at the boundary layer, $I_{L0}^{\downarrow}$ modified by $\xi_L^{\downarrow}$ a reduction factor given by (19). This is based on the Beer-Lambert law (see equation (10)) for transmission through a turbid medium where k is the extinction coefficient and LAI is the leaf area index or the total single sided leaf area per unit ground area. The second term accounts for the contribution from the tree canopy above, where ε_f and T_f are the emissivity and average temperature of the canopy, respectively. The last term accounts for the longwave radiation from surrounding surfaces, where Ψ is the SVF, ε_w and T_w are the emissivity and average temperature of the walls, respectively (Huttner 2012).

Additionally, there is also a body of research regarding the radiation budget in forest canopies. (Essery, et al. 2008) note that while canopies reduce shortwave radiation during the day, longwave radiation is larger due to the foliage heated by solar radiation.

Furthermore, during the night the canopy is generally warmer than the sky. They give the following formula for downward longwave radiation,

$$I_L^{\downarrow} = \Psi I_L^{\downarrow,0} + (1-\Psi)\sigma T_f^4 \qquad (20)$$

where Ψ is the sky view factor for the point under the canopy, $I_L^{\downarrow,0}$ is the unobstructed longwave radiation, and T_f is the canopy temperature. To simplify matters, it can be assumed that the effective canopy temperature is equal to the air temperature, T_a. This equation differs from (18) in that the emissivity is assumed to be 1, there is no term for built obstructions, and, more interestingly, the reduction factor (19) based on LAI is replaced by the SVF. (Essery, et al.) go on to study this relationship between SVF and LAI in forest canopies and find that it corresponds to an equation similar to the Beer-Lambert law

$$\Psi = e^{-\Omega LAI} \qquad (21)$$

where Ω is an empirically derived coefficient called “clumping factor.” It is worth noting that this relationship has been established in forestry applications where the only obstructions are trees. In urban micro-climate simulations, the presence of buildings and other built structures must also be accounted for in the SVF term.

2.3.3. Other Effects of Trees

As well as their roles in radiation exchange, trees contribute to the urban micro-climate in many additional ways. They provide evaporative cooling, reduce storm water runoff, protect against flooding, decrease noise, sequester carbon, decrease wind speeds, and absorb both particulate and gaseous pollution such as NO_x, SO_x, and O_3 (Ennos 2012 & Akbari, et al. 2001).

The largest contribution of trees to the urban climate other than the interception of solar radiation, is the cooling effect of evapotranspiration. Of the radiation absorbed by leaves, part is used in photosynthesis and part is converted into heat. Some of this heat is dissipated back into the environment as sensible heat through convection and radiation (Block, et al. 2012). However, a large portion of this energy is converted into latent heat in the process of evaporation. (Oke 1987) examines the diurnal energy balance of two coniferous tree stands and finds that this latent heat flux accounts for between one-third and two-thirds of the total.

Quantifying the effect of evapotranspiration made difficult by the large number of factors on which it depends. A short list includes temperature, humidity, wind speed, stomatal conductance, leaf area index, and leaf height (Ennos 2012). Although it falls outside the scope of this paper, an effort by Ennos to parameterize evapotranspiration based on sequestered biomass (i.e. tree growth) could be readily combined with a city's tree registry if it contained historic data regarding tree crown area and trunk diameter.

In addition to their environmental impacts, trees play a vital role in the aesthetics of the built environment and contribute to recreational satisfaction (Attwell 2000). Furthermore, property values are higher along streets with more trees and shopping areas with landscaping do more business than those without (Gartland 2011).

2.4 Other Factors Influencing the Urban Climate

In addition to increased absorption of shortwave solar radiation and decreased longwave radiation loss compared to rural areas, the urban microclimate is also effected by the presence of anthropogenic heat sources, pollution, materials with increased heat storage, and the reduction of windspeed by buildings (Oke 1987).

Furthermore, the removal of vegetation and the prevalence of water-tight construction materials reduces the amount of evapotranspiration (Gartland 2011). This means more of the energy in the urban system will be converted to sensible heat and thus contribute to the UHII (Oke 1987).

Urban geometry tends to reduce wind speeds and thus convective heat transport. (Landsberg 1981) cites several empirical studies that show reductions in wind speed due to urbanization as high as 60%, but mostly in the range of 20% to 40%. Slower wind reduces heat loss at night and increases storage during the day (Gartland 2011).

Anthropogenic heat is the term given to heat energy generated by human activity. This includes sources such as vehicles, buildings, industry, as well as the metabolic output of humans. (Oke 1987) gives estimates of anthropogenic heat output for a variety of cities based on per capita energy use and population density. These numbers range from 3 to 265 $W.m^{-2}$ and show high seasonal variation in cold climates.

Higher levels of pollution in urban areas lead to a greater amount of particulate matter in the atmosphere. This particulate matter will absorb a greater portion of the incoming shortwave radiation and can lead to reductions of up to 30%. This absorbed energy is then reemitted as heat energy causing increases in the amount of downward longwave flux from the atmosphere (Oke).

3 Methodology

3.1 Overview

The core of this work centers around the use of an algorithm for calculating the shadows cast by obstructions modelled in a 2.5 dimensional digital elevation model (DEM). These models are 2D raster images with heights encoded in the value of each pixel. This is a common method for representing the geometry of large urban areas and terrain.

This algorithm is then adapted to calculate maps of both SVF and global irradiance in the urban environment based on a simplified version of the SOLWEIG-model. This section describes the implementation of these algorithms, the methods used to validate them, and the input data used for calculation.

3.2 Study Areas and Input Data

3.2.1. Weather data

For this study, five urban study areas were selected. Each is centered around weather stations located in the city of Vienna, Austria. Three of the stations are maintained by the Zentralanstalt für Meteorologie und Geodynamik (ZAMG) and two by the City of Vienna. The data provided included hourly temperature values for years 1985 to 2012, however not every station has been active for that entire time period.

In addition, there are four rural weather stations in the area immediately outside the city (see fig. 5). Before 1997, there is only data for the weather station in Seibersdorf (labeled “SEI” in fig. 5). However, when compared to the maximum, minimum, and mean values of the other stations in the more recent years, it was found that there was little variation in the values (e.g. winter season, fig. 6). Therefore, as it has the most complete record, Seibersdorf was chosen as the rural reference station for the purpose of calculating UHII.

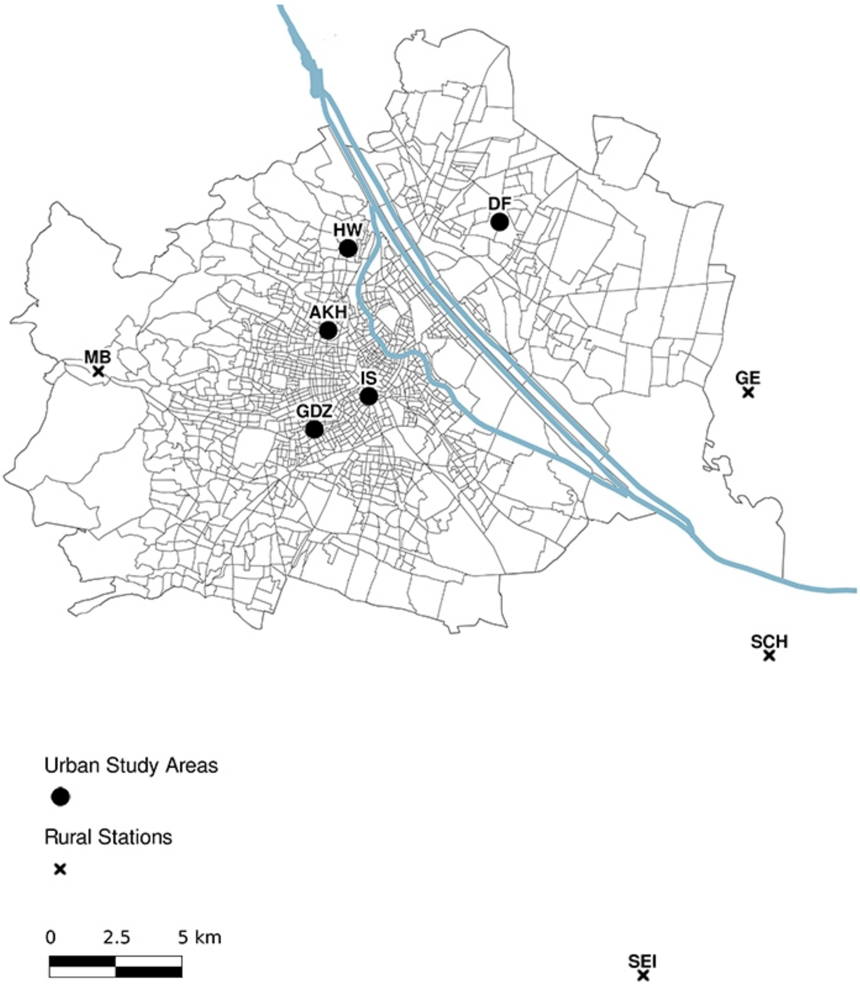

Figure 5. *Study areas and rural reference stations in Vienna, Austria*

As this research is aimed at studying the effect of trees, the data was filtered to include only the summer and winter seasons (i.e. full foliage and defoliated periods). In order to capture the defining climatic conditions of each season, a midseason month was defined as the 15 days preceding and the 15 days following the middle day of the season. The specific date ranges are found below in table 1.

Table 1. *Midseason months*

Season	Start	End
Winter	January 20th	February 19th
Summer	July 21st	August 20th

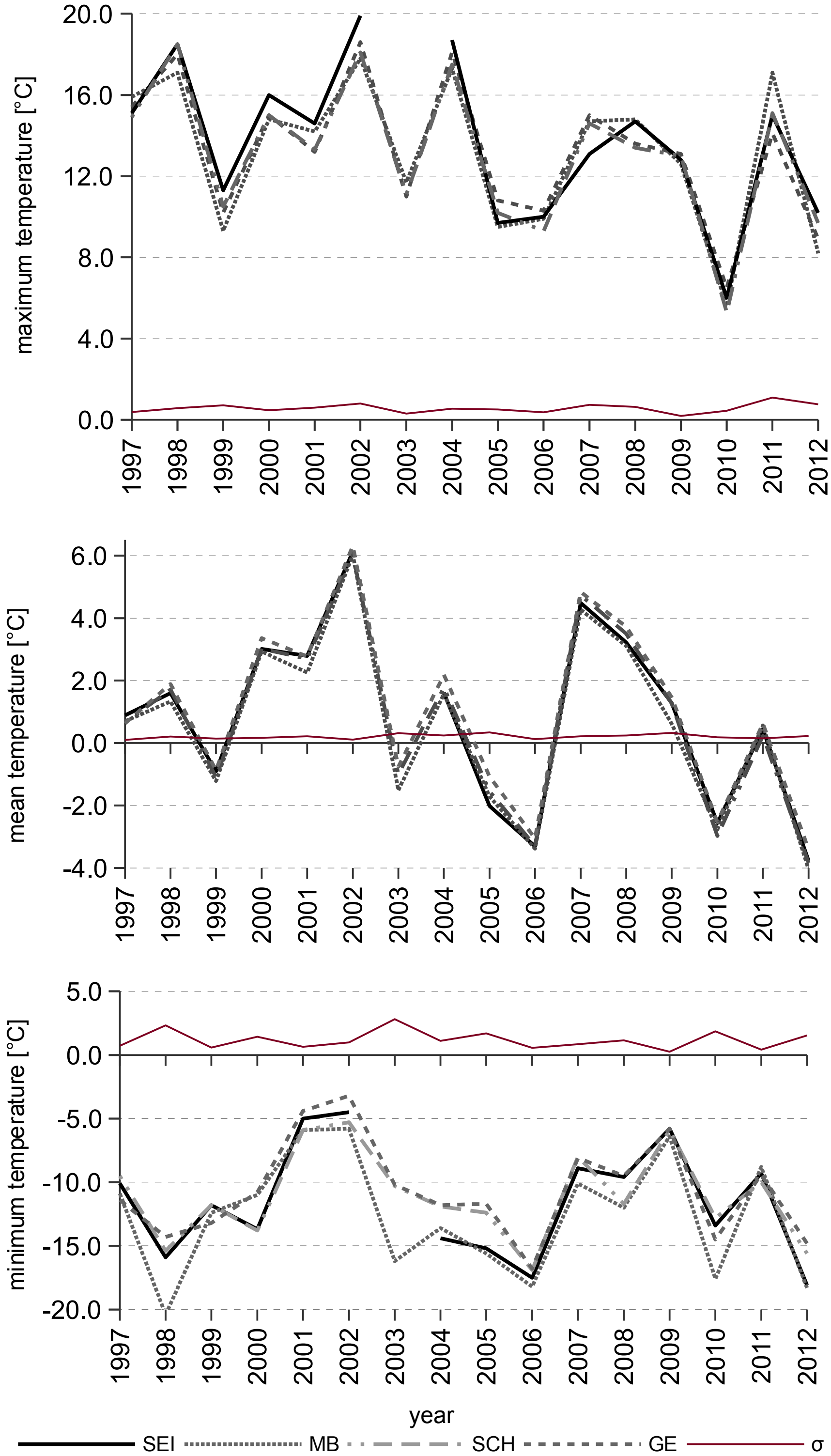

Figure 6. *Comparison of rural station average maximum (top), mean (middle), and minimum (lower) values for the winter season since 1997.*

Due to the strong diurnal pattern of the UHII, the data was further categorized by time of day. The UHII typically reaches its highest values after sunset. This is due to the city retaining heat, while the rural reference area cools at a much faster rate. During the day, on the other hand, obstructions to direct solar radiation in a city can potentially create cool islands. As the time of sunset varies throughout the year, each season was given a different range (see table 2 and fig. 7).

Table 2. *Diurnal classification by season*

Season	Classification	Start	End
Winter	Day	10:00	15:00
	Night	18:00	07:00
Summer	Day	08:00	17:00
	Night	20:00	05:00

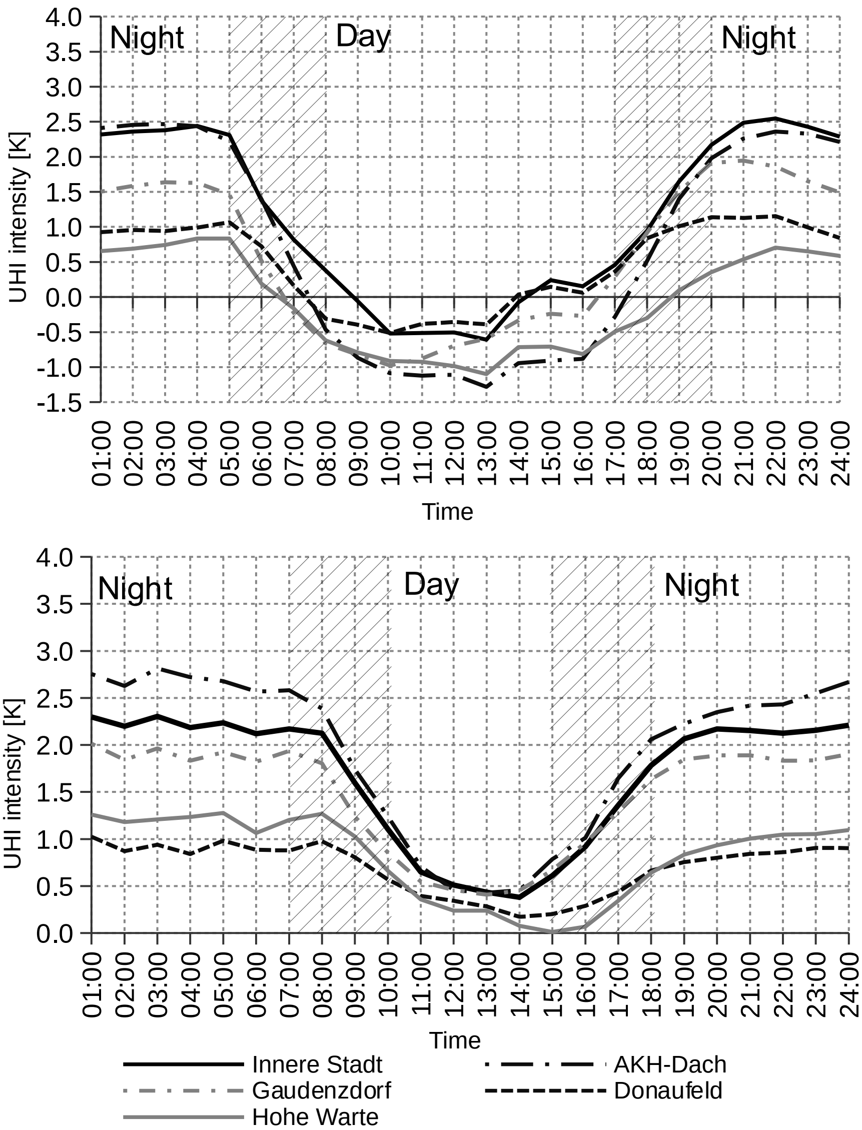

Figure 7. *Mean hourly values of UHII for summer (top) and winter (bottom).*

The weather data was received in a raw format and had to be cleaned of null and error values. Additionally, in order to preserve as much of the historical data as possible, gaps of less than 6 hours in the recorded values were interpolated from the values on either side of the gap as well as the values at corresponding times from immediately adjacent days. In the event that the gap was larger, that season was removed from the data set.

Interpolation was handled such that it worked from either end of the error range towards the middle. Each value was determined by the weighted sum of two estimates: the linear interpolation of the 4 values preceding or succeeding the missing value (depending on the direction it was working) and the mean of measurements at corresponding times on the 3 days before and after. The weight varies so that the linear interpolation is prioritized at either end where it is closer to measured values. The weighting of the linear interpolation decreases towards the middle such that the typically sinusoidal variations of the diurnal cycle can be accounted for by the comparison to values at the same time of day on the immediately adjacent days.

For the validation of the solar irradiance algorithm, measures of diffuse and global radiation from the Department of Building Physics and Building Ecology's (BPI) weather station were also used. This weather station is installed at the top of a tower at the Vienna University of Technology at the height of approximately 40 meters above the surrounding terrain (210m above sea level) (see fig. 8). The horizontal irradiance was measured with a Delta-T SPN1 Sunshine Pyranometer at 1 minute intervals. This instrument uses an array of seven thermopile sensors in combination with a computer-generated shading pattern to separate the direct and diffuse components of incident solar radiation. It is rated with an accuracy of ±8% / ±10 $W.m^{-2}$ (Delta-T 2013).

Figure 8. *BPI Weather Station*

Additionally, the SOLWEIG model uses direct normal irradiance (DNI) as an input rather than the direct component measured at a horizontal surface, therefore it was necessary to calculate this value. The Delta-T company provides a suite of functions to calculate the DNI from the measurements of an SPN1 Sunshine Pyranometer installed horizontally. It uses the following equation

$$DNI = \frac{(I_G - I_{dif})}{\cos(\phi)} \quad (22)$$

where I_G is the global irradiance, I_{dif} is the diffuse fraction, and ϕ is the zenith angle. Furthermore, to limit the large overestimates created by this calculation when the sun is at the horizon, the cosine factor is gradually reduced to zero for zenith angles between 88° and 90° (Wood 2012).

3.2.2. Geospatial data

A circular area with a radius of 350 meters from the urban weather stations was defined as the extent of the study areas in accordance with recommendations from (Stewart and Oke 2012). For each of the five areas, three georeferenced data files were obtained from the city of Vienna:

1. A DEM including all buildings, trees, and obstructions at a resolution of 0.5m. This kind of file is also called a digital surface model or DSM (see fig. 10a).
2. A DEM including only terrain information (i.e. a digital ground model or DGM) at a resolution of 1m (see fig. 10b).
3. A vector file representing each distinct feature of the area as a polygon classified by land use type (see fig. 10c).

The DSM was used without modification as the model representing the city including the tree canopy. A treeless DEM was created for comparison to this detailed DSM. This was a three step process. First, the vector file from the city was used to select all the polygons representing buildings. Then, a 1.5 meter buffer was applied to account for the pixelation of building facades at diagonals to the DEM grid. Finally, the information from the DSM within the buffered vectors was combined with the DGM to produce a DEM containing only buildings.

As the DSM was created from a single lidar scanning event, there are many artifacts resulting from vehicles and temporary structures, such as construction cranes and street cars (see fig. 9). The effect of these “ghosts” is very localized as compared to the size of the study area. As such, it is likely the impact on area averaged values is not significant. However, as will be seen later, this did interfere with some comparisons to field measurements. No effort was made to manually clean the DSM provided by the city government and automated methods for removing this noise fall outside the scope of this paper.

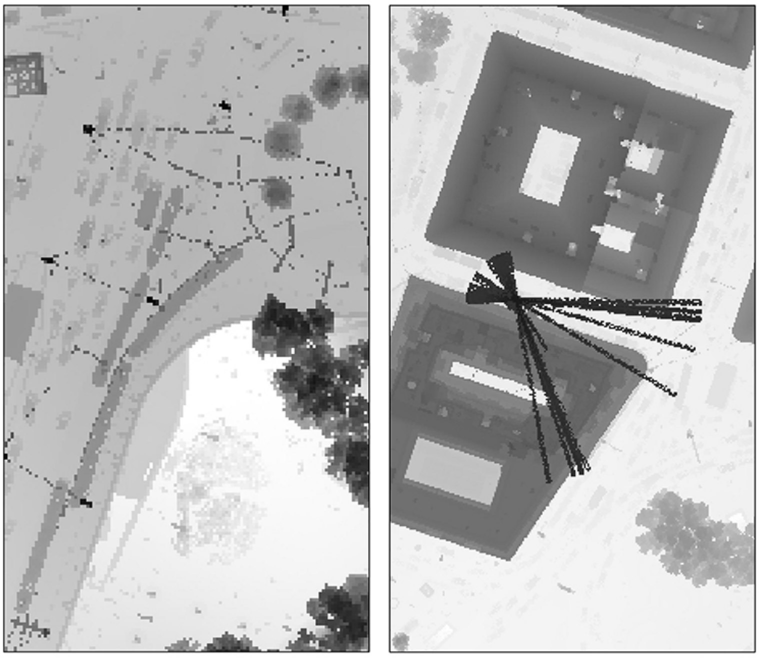

Figure 9. *Examples of lidar noise in DEM. Streetcars and overhead wires (left) and a rotating construction crane (right).*

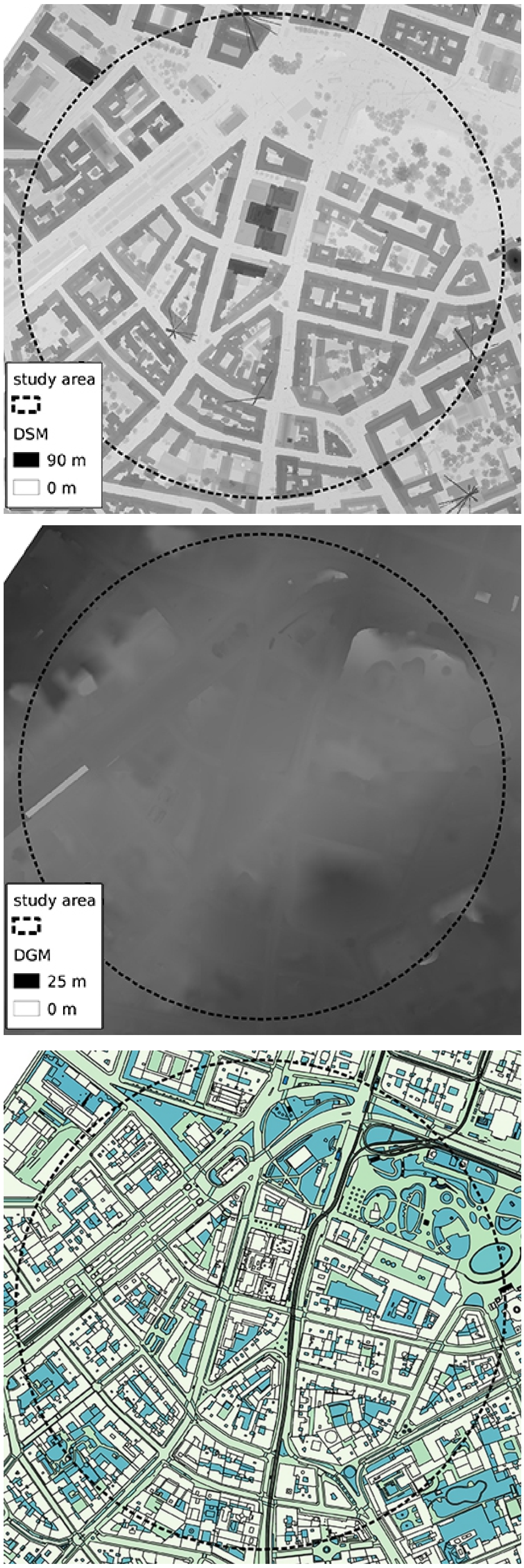

a)

b)

c)

Figure 10. *City Data : DSM (a), DGM (b), land-use vector (c).*

3.3 Sky View Factor

3.3.1. Shadow Casting Algorithm

In order to calculate SVF values for the selected study areas in Vienna, the first task was to implement an algorithm in Quantum GIS (QGIS 2013). The continuous shadow casting method developed by (Richens 1997) was chosen and is described below.

This algorithm calculates the shadow volume created from a hypothetical light source by iteratively offsetting and decreasing the height of a DEM. A shadow volume, as represented in a DEM, is encoded as the height of “the upper surface of the volume of air that is in shadow” (Richens 1997). In other words, a pixel in the original DEM that has a height value less than the shadow volume is considered to be in shadow (see fig. 11).

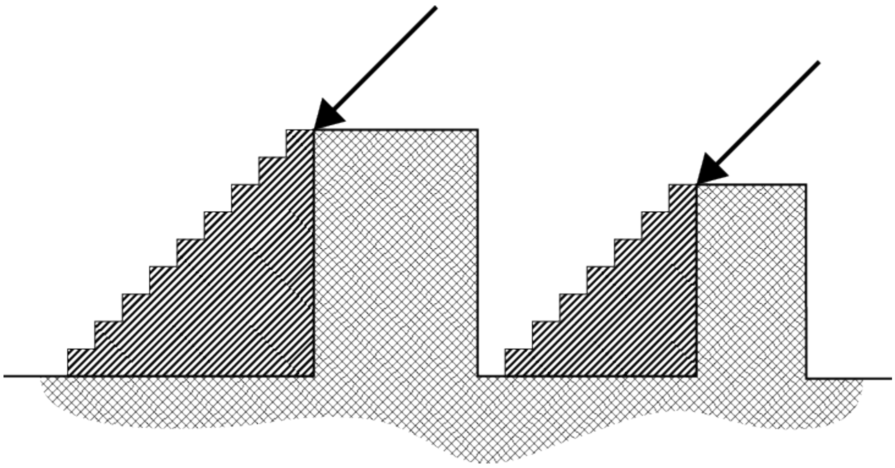

Figure 11. *Cross-section of a shadow volume as represented in a DEM.*

First, the vector from the light source is defined by its x, y, and z components. Then the DEM is offset by the x and y values and the z component is subtracted from the height. The shadow volume is constructed by iterating this process and combining each new result with the cumulative total by selecting only the maximum value for each pixel. This is converted into a shadow map by calculating the difference between the shadow volume and the original DEM. Pixels with a height value greater than zero are considered to be shaded and the others receive light (see fig. 12).

In order to calculate SVF, this process is then repeated for a large number of light sources (e.g. 1000, in this study) spread across the sky hemisphere with a cosine-weighted distribution. The SVF for each pixel is the fraction of the number of times it receives light to the total number of light sources. In other words, a pixel that is lit by every light source has a SVF of 1 (i.e. an unobstructed view of the sky) and pixel that is always in shadow has a SVF of 0.

In previous studies this algorithm has been validated both by comparison to hemispherical photography (Lindberg 2005) and simplified geometries with known mathematical solutions (Brown, et al. 2001). One limitation of this method is that there will always be significant errors of over estimation at the margins of the result SVF map. This occurs because the input DEM will always have some boundary beyond which there is no information and thus no obstructions of the sky. This can be avoided by using DEM maps with a buffer around the area of interest (refer to fig. 10).

Figure 12. *Example shadow map. Resselpark, Vienna.*

Using this technique it is possible to set the height of the virtual sensor and thus produce a continuous SVF map at varying heights. For the purposes of validation, the SVF maps were calculated at the height of the fish-eye camera (1m). However, the SVF maps created for examining the relationship to UHII were calculated at ground level (0m) as Svensson (2004) has shown that SVF at ground level has a stronger correlation with UHII.

3.3.2. Hemispherical Photography

Steyn (1980) first described the application of hemispherical photography to calculate view factors in “complex radiation environments” such as urban canyons. Since then it has seen wide use in urban (Bärring, et al. 1985, Brown, et al. 2001) and forestry (Holmer, et al. 2001, Essery, et al. 2008) applications. In this study, hemispherical photography was used to measure on site SVF values, which were then compared to the algorithmically generated values. Between 12 and 16 photos were taken at each of the 5 study areas with a Nikon Coolpix 8400 with a FC-E9 Fisheye Converter lens (183° field of view). The camera was mounted and leveled on a tripod at the height of 1 meter and pointed directly at the sky.

These photos were then processed using the Sky View Factor Calculator version 1.1 created by the Göteborg Urban Climate Group and based on the work of Holmer, et al. (2001) and Johnson and Watson (1984) This software distinguishes between sky pixels and obstructions (see fig 13). The photographs were taken between the 6th and 23rd of June, 2013.

Camera positions were determined with a combination of geolocating with a Holux GR-213 GPS Receiver (1-5 meter position accuracy) and dead-reckoning from field notes and satellite imagery. Geolocation alone was insufficient because the accuracy of the device and the value being measured are directly related. In other words as SVF decreases so does the position accuracy of the GPS device.

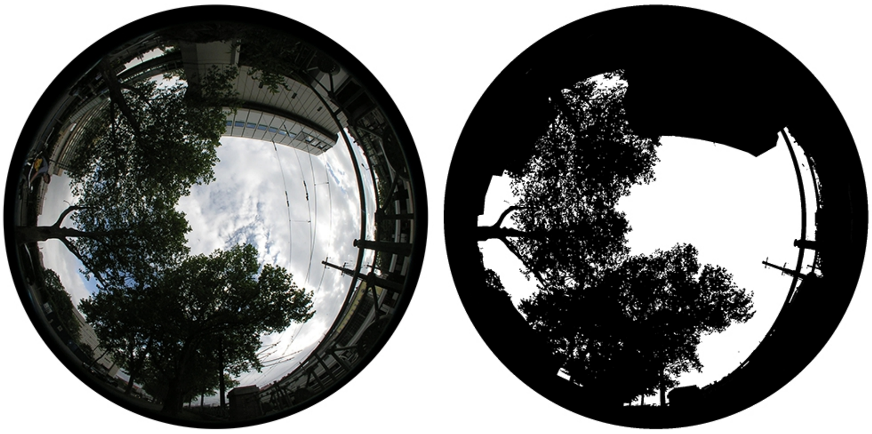

Figure 13. *Hemispherical photograph (left) and post-processed image for SVF calculation (right).*

3.3.3. Area mean sampling methods

It is common in the literature comparing UHII and SVF to characterize the SVF of a location by using an “areal mean”. However, the meaning of this term is far from standard. In (Unger 2004) this refers to the average of SVF estimates from theodolite readings at a height of 1.5m along the study's measurement transect. In (Gál, et al. 2009) SVF is calculated algorithmically from a digital model at ground level and averaged over 500m x 500m square cells with buildings excluded. In (Chen, et al. 2012) a similar computational method is used to find the mean SVF at ground level with buildings masked for circular areas with various radii (50, 100, 150 and 200m).

Lindberg (2007) is one of the few studies to seriously compare different methods of taking the areal mean. That study compares entire area means including buildings to those using only the ground surface. Additionally he proposes an interesting, but computationally intensive, integrated vertical mean measure of SVF. In this study it is determined that there is actually a slight increase in the strength of UHII-SVF relationship when buildings are included.

The best method to distill measurements of a continuous SVF map into one representative value for an area remains an open question. Therefore, this study examined 3 land-use classification filters used in combination with 4 distance weighting methods to take area means of the resulting continuous SVF map.

The most simple of the 3 land-use filters is a whole area mean, which samples pixel values from the entire circular study area. However, urban micro-climate studies are primarily concerned with the effects within the Urban Canopy Layer, that is to say, below the level of building roofs. In order to better represent that condition, another land-use filter was employed to filter out the values at building locations. Additionally, as some studies only measure along mobile transects, a third filter was used to select only values coincident with public streets.

Furthermore, as these values are ultimately compared to the air temperature measurements from a fixed weather station, it could not be assumed that each pixel should be given equal weight to determining the overall SVF number. To test this relationship, 4 distance weighting were studied: the unweighted mean, the inverse square, the inverse, and the inverse of the square root (see fig. 14).

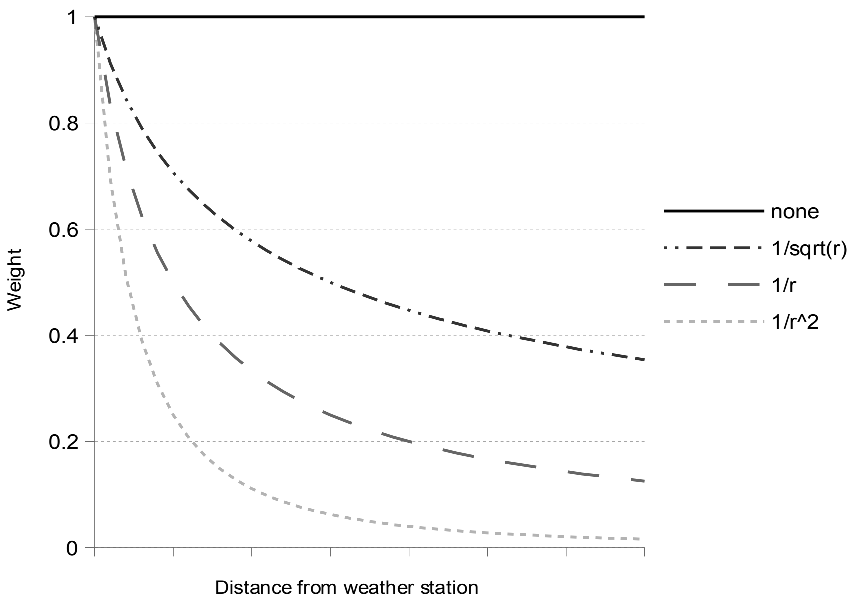

Figure 14. *Distance weighting curves*

In an effort to compare the effects of including tree canopy information, these sampling methods were used both with the building only DEMs and DEMs including the tree canopy. This resulted in 24 values for each of the 5 study areas. Simple linear regression was then used to determine the strength of the relationship between these different measures of SVF and UHII.

A key assumption in using the historic weather data paired with SVF values calculated from current DEMs is that the areal mean of the SVF is fixed over the time period. For most areas in the study this is a safe assumption, as building density has changed very little in the central areas of Vienna in the last decades.

The AKH study area is centered on Vienna's Allgemeines Krankenhaus (General Hospital) and the character of this area was dramatically changed by the construction of the large medical facility. However, the weather data for this area starts only after the completion of the project. Since that time the area has changed little in terms of building density.

Of all the locations, the Donaufeld study area (labeled “DF” in fig. 5) has likely seen the most change over the study period and the assumption that SVF has remained fixed may account for some error. However, even at current levels of building density it is the most open of the five areas with an area mean SVF of 0.66‡ including trees. Assuming that building density has increased during the measurement period, one would expect to see an increasing trend in UHII. However, as is clear in figure 15 below, this is not the case.

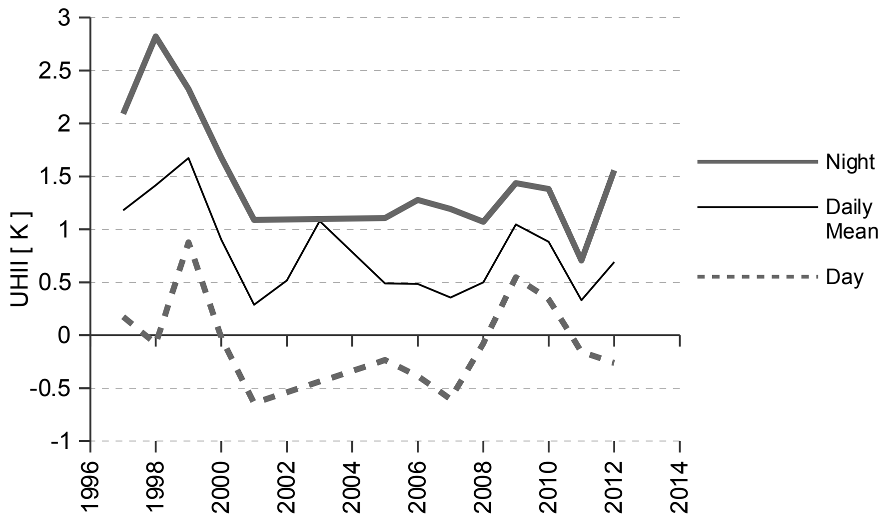

Figure 15. *Summer season UHII values for the Donaufeld study area.*

‡ Averaged across all sampling methods

3.4 Shortwave Radiation

3.4.1. Algorithm Adaptation

In order to capture the shortwave solar radiation incident on a point, at a given time it is necessary to calculate three terms: the direct, the diffuse, and the reflected components. This study adapts a simplified formula from Lindberg (2007):

$$\begin{aligned} I_G = \; & I_{mDr}\, S_{ij} \sin(h) + I_{mDf}\, \Psi_{ij} \\ & + (1-\Psi_{ij})\, I_{mG}\, \alpha \sin(h) \end{aligned} \tag{23}$$

The first term on the right hand side of the equation describes the direct component where I_{mDr} is the measured DNI, S_{ij} is a binary value for a location i, j that describes if it is in direct sun [1] or in shade [0], and h is the altitude angle of the sun. The second term describes the diffuse radiation where I_{mDf} is the unobstructed measure of diffuse radiation, and Ψ_{ij} is the sky view factor at the given location as calculated in section 3.2.1. This treatment assumes an isotropic sky condition. The third term is a simplified estimation of the reflected component, where I_{mG} is the measured global radiation, α is the average albedo of the area, $(1 - \Psi_{ij})$ represents the amount of nearby obstructions, and $\sin(h)$ represents their availability "for reflection throughout the diurnal circle" (Lindberg 2007).

To account for the presence of trees, equation (23) was adapted as follows for the direct component:

$$\begin{aligned} I_{dir} = (I_{DirHorz}\, S_{ij}) \\ \times ((Str_{ij} + (1-Str_{ij}) f_s)(1-C_{ij}) + f_s\, C_{ij}) \end{aligned} \tag{24}$$

where $I_{DirHorz}$ is the measured value of the direct component on a horizontal surface, S_{ij} is a binary value for the shade computed without trees and Str_{ij} is a binary value for the shade computed with trees, f_s is the fraction of radiation intercepted by the tree canopy, and C_{ij} is a boolean value defining whether the pixel is directly under the tree canopy [1] or not [0]. In other words, if a point is shaded by a building the direct component is zero. If it is under the canopy or in the shade of a tree, the direct component is reduced by the shading factor. Otherwise, the point receives the entire direct component. The sine of the solar altitude angle is removed, because the input for the direct component used in this model is the horizontal irradiance rather than the DNI. Therefore, the vector decomposition is unnecessary.

The diffuse component is given as:

$$I_{diff}=I_{mDf}\left(\left(\Psi_{tr}+\left(\Psi_{bg}-\Psi_{tr}\right)f_s\right)\left(1-C_{ij}\right)+\Psi_{bg}\ f_s\ C_{ij}\right) \tag{25}$$

where Ψ_{tr} and Ψ_{bg} are the sky view factors calculated from the DEM with trees and without, respectively. In effect, if the point is under the canopy, the diffuse component is reduced by the SVF accounting for the obstructions of buildings and the shading factor. Otherwise, the portion of the sky obstruction due trees is found by taking the difference of Ψ_{tr} and Ψ_{bg}. Then, this portion of the diffuse component is further reduced by the shading factor and added to the portion diffuse component from the completely unobstructed sky.

The reflected component as:

$$I_{ref}=\left(\left(1-\Psi_{bg}\right)\ I_{mG}\ \alpha\ \sin\left(h\right)\right)\left(\left(1-C_{ij}\right)+f_s C_{ij}\right) \tag{26}$$

and finally:

$$I_G=I_{dir}+I_{diff}+I_{ref} \tag{27}$$

The result is similar to (12) from the SOLWEIG model, but if differs in a few respects. In this adaptation, Ψ_{tr} is the SVF calculated with both trees and buildings, whereas Ψ_v in (12) is the SVF calculated with trees only. This makes little difference in the calculation of incident shortwave radiation, but the separation is important in the calculation of longwave radiation (see equation (17)).

The primary difference is the boolean array describing the presence or absence of the tree canopy, C, is calculated from the geospatial dataset in the following steps:

1. The DGM is subtracted from the DSM leaving a DEM with height values of all obstructions above ground.
2. Then a filter is applied to only select those obstructions with heights above 3m. This removes low obstructions and much of the noise from the lidar generated DEMs.
3. The land use vector layer is used to remove the building areas from resulting DEM.

In other words, all objects in the DSM that are taller than 3m and not buildings are considered to be trees. As mentioned above, artifacts of vehicles and temporary structures are present in the DSM. This method removes many, but not all such anomalies, which can introduce some significant localized errors. However, at the scale of the entire study area this method appears adequate to define the areas covered by the tree canopy (see fig. 16).

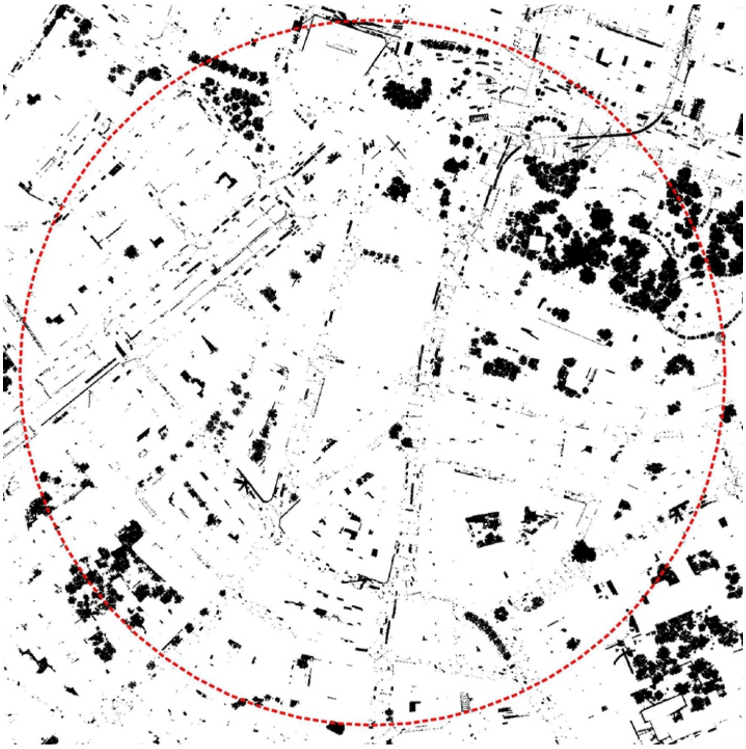

Figure 16. *Tree canopy map boolean map – the black pixels indicate the presence of the urban tree canopy.*

This treatment is necessary because of the simplified representation of trees in DEMs (see fig. 17). They are treated as extruded monolithic volumes and there is no account of the volume under the canopy without foliage (i.e. the trunk zone). As a result, for pixels in the tree canopy zone, Ψ_{tr} is calculated at the top of the tree canopy. If this were used as the SVF at ground level, it would be an extreme overestimation. The inclusion of boolean array C, assumes that these areas are always subject to the complete shading factor reduction for all three components of shortwave radiation. This results in an underestimate of irradiance, particularly at low sun angles. Furthermore, this poor geometric representation of trees also results in an overestimation of the number of pixels in the shade of the tree (Str_{ij}).

In the most recent SOLWEIG model this particular source of error is overcome by using two DEMs to describe the vegetation. One which captures the upper canopy surface and another which describes the height of the trunk zone (see fig. 17). (Lindberg and Grimmond 2011) modify the shadow casting routine detailed above such that pixels are only counted as shaded when the shadow volume created by the upper canopy is above the DSM and the shadow volume of the trunk zone is below. In essence, the trunk zone DEM is used to carve out the volume that is lit beneath the canopy (see fig.18).

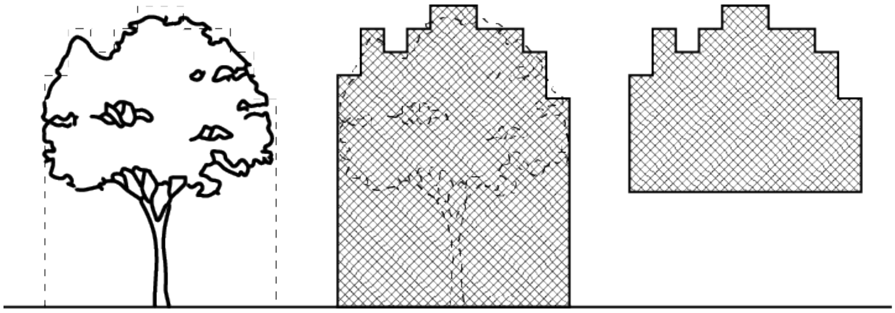

Figure 17. *Cross-sectional representation of a typical tree (left) in a standard DEM (middle) and in SOLWEIG (right).*

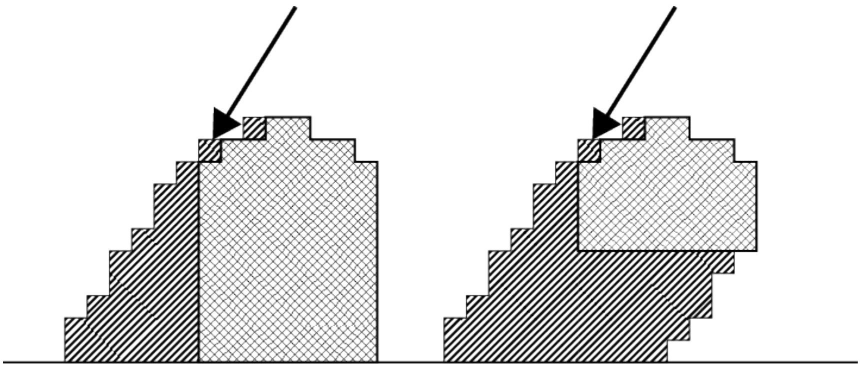

Figure 18. *Shadow cast on a standard DEM tree (left) and a tree as represented in the SOLWEIG model (right).*

In order to determine one representative shading factor, f_s, for the area, the tree registry of the city was sorted by genus to identify the most common trees. In Vienna, trees belonging to the genus *Acer*, or maples are by far the most prevalent (see fig. 19). Then four values for different species of maple were taken from (Nowak 1996) and averaged for a value of 0.858 (see table 3). The average value of albedo for an urban area was taken as 0.15 according to (Oke 1987).

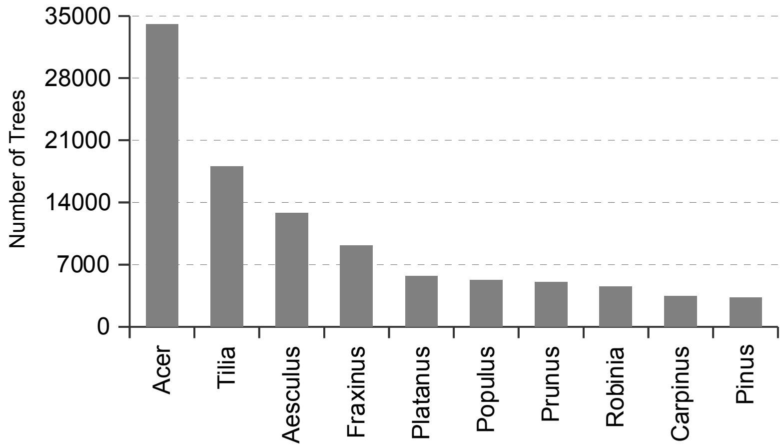

Figure 19. Tree genus distribution in Vienna, Austria

Table 3. *Average shading factors (derived from Nowak 1996)*

Tree species	Shading factor
Acer Ginnala Maxim.	0.91
Acer platanoids L.	0.88
Acer rubrum L.	0.83
Acer saccharinum L.	0.83
Acer saccharum Marsh.	0.84

3.4.2. On-site measurements

In an effort to study the accuracy of this method for estimating the shortwave radiation exchange, measurements of global irradiance where taken throughout the Innere Stadt study area in the vicinity of the BPI weather station. The measurements were taken both directly under tree canopies and in a variety of open sky conditions.

The measurements under the canopies were taken with 3 Schenk model 8101 Star Pyranometers mounted on tripods at 1 meter (see fig. 20). Values were logged at 1 minute intervals using a AHLBORN ALMEMO 2590 data logger. To better account for the high spatial variation in solar radiation beneath tree canopies (Hardy, et al. 2004), these pyranometers were repositioned and re-leveled every 15 minutes and an averaged value used for each time step (see fig. 21). The observation periods for these measurements were August the 22nd and September the 19th, 24th, and 28th, 2013.

Figure 20. *Pyranometer under tree canopy*

It is worth noting that the summer had been exceptionally hot and by this point in the season many of the trees were suffering from severe heat-stress. This will have the effect of reducing the leaf area and shading effect below standard value used in the model. This should result in some under prediction of measured values.

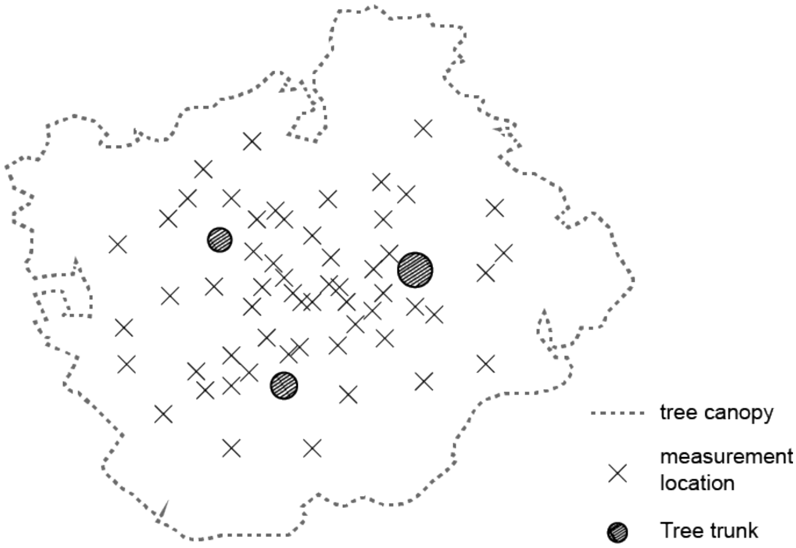

Figure 21. *Pyranometer positions during one measurement session*

In open sky conditions, a single Schenk model 8101 Star Pyranometer, mounted on a tripod at 1 meter, was used at fixed locations. Values were logged at 1 minute intervals with an AHLBORN ALMEMO 2590 data logger. Data collection was performed over 4 days in July 2013 over periods of 45 minutes.

3.4.3. Calibration

Following the measurement periods, the pyranometers where positioned at the Department of Building Physics and Building Ecology's weather station for a 7 hour period with clear skies. The data from this period was logged at 1 minute intervals and compared to the global irradiance values measured by the station's Delta-T SPN1 Sunshine Pyranometer.

Over this period, the deviation in the Schenk pyranometers from the recently calibrated Delta-T pyranometer was fairly constant (see fig. A1 in the appendix). A calibration factor was determined for each instrument from the average of this error over the time period (see table 4). Figure 22 shows the cumulative error before and after the calibration. There is a noticeable improvement with 50% of the values after calibration having an error less than 2% for all sensors. Note that from 10:44 until 11:31, the pyranometers were shaded by another instrument on the weather station. These values were removed from the calibration dataset.

Table 4. *Instrument calibration factors*

Instrument #	2228	2227	1260
Calibration factor	4.97%	2.74%	2.08%

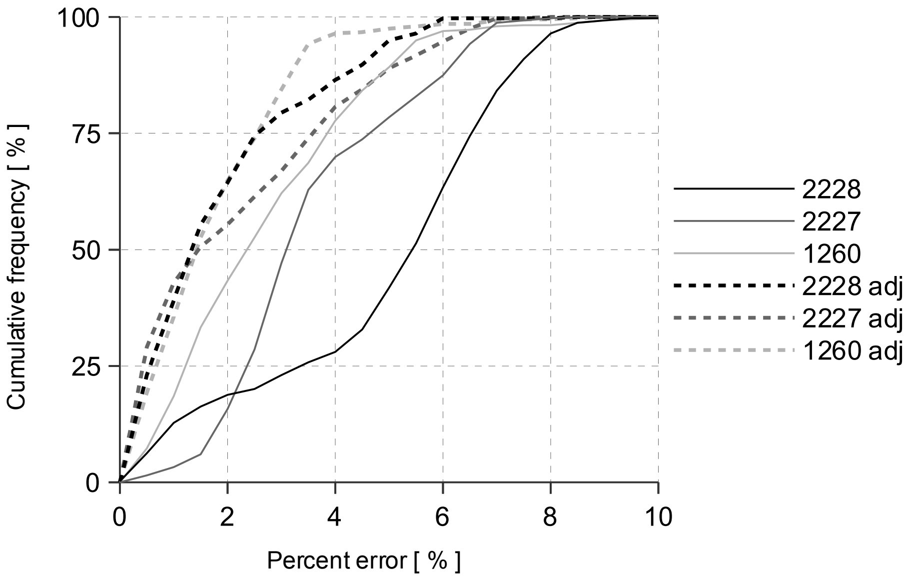

Figure 22. *Cumulative error distributions for sensors before (solid lines) and after (dashed lines) calibration.*

4 Results

This chapter summarizes the results of the study. The first section presents the data regarding SVF: the validation, sampling methods, and correlation with historic UHII vales. This is followed by the results relating to the shortwave irradiance algorithm and the field measurements.

4.1 Sky View Factor

The SVF algorithm produced continuous SVF maps at a resolution equal to the input data. In this case, the output was an image of each study area with a SVF value for each 0.5m x 0.5m area. Examples both with and without trees can be seen in figure 23 below.

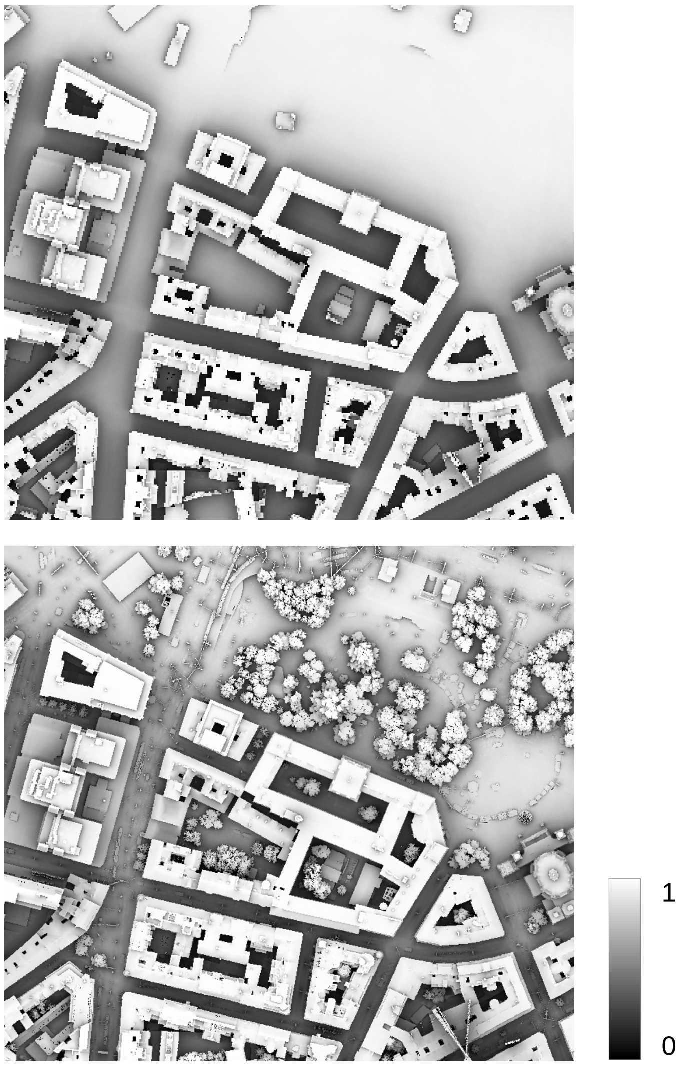

Figure 23. *Sky view factor maps without trees (top) and with trees (bottom).*

4.1.1. Validation

When the georeferenced SVF measurements taken in the field were compared against the points sampled in those same locations from the algorithmically derived continuous SVF maps, it became apparent that there were several outliers (see fig. 24). Examining these points in further detail it was discovered they could be classified into 3 groups, each representing a particular type of error: points coincident with canopies, points strongly influenced by canopies, and points strongly influenced by DSM artifacts (see figs. 25 and 26).

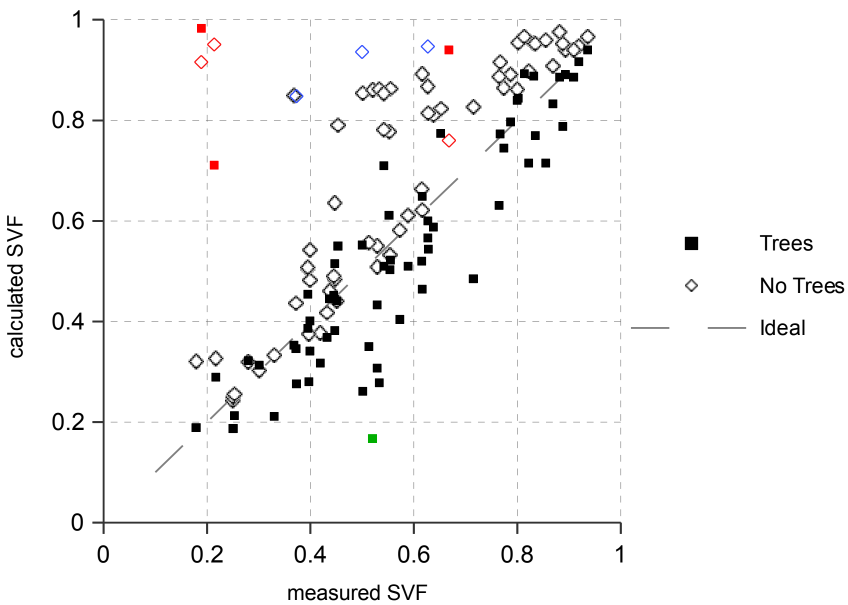

Figure 24. *Calculated SVF versus measured SVF with outliers highlighted – coincident with canopies (red), influenced by canopies (blue), influenced by DSM artifacts (green).*

The points coincident with the canopies represent a fundamental error in the representation of trees in DEMs, namely as monolithic objects that completely occupy the volume below the canopy (as discussed previously in section 3.4.1). Therefore, the SVF value calculated at these points from DEMs with tree information represents the SVF at a point above the canopy rather than below it where the measured value is taken. This results in a significant overestimation of the measured SVF. Unsurprisingly, these locations are also poorly predicted by the SVF values generated without tree information.

Those locations that are strongly influenced by tree canopies are points where the majority of the sky is obstructed by trees. The extreme variation in these cases is only exhibited in the SVF map created without tree canopies. These points are well represented by the SVF with tree information and therefore they clearly highlight the difference between the two SVF maps.

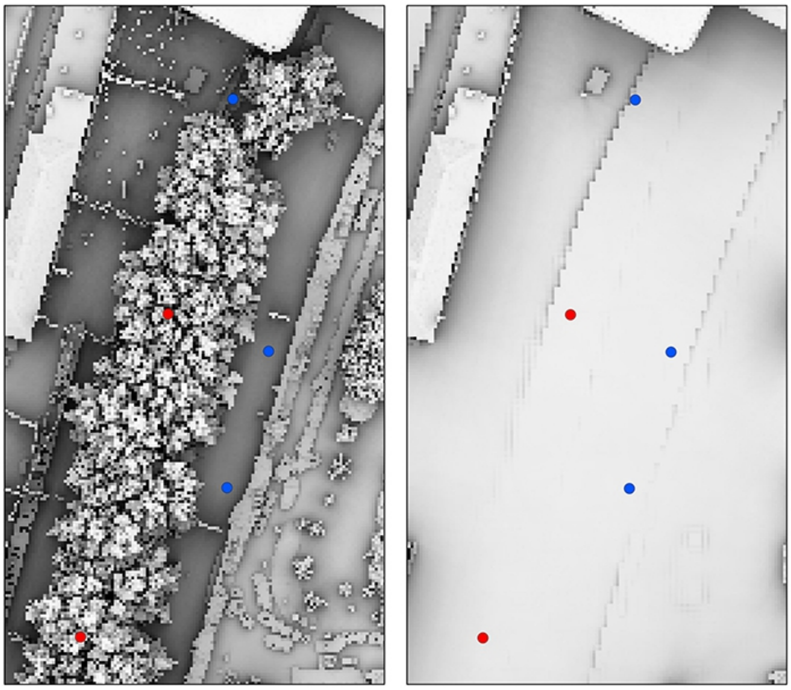

Figure 25. *SVF outlier locations coincident with the canopy (red) and strongly influenced by the canopy (blue) shown on the map with canopy information (left) and without (right).*

On the other hand, due to the process of their creation (see section 3.2.2.), the treeless DEMs have far fewer lidar artifacts. Therefore, the error represented by the third class of outlier is limited to the SVF maps created from DEMs with trees. Figure 26 shows the outlier's location in the SVF map, as well as the corresponding obstruction mask created from the hemispherical photograph taken at that location. An overhead support for streetcar cables can be seen as a thin line projecting from a street lamp on the mask. However, in the DEM this feature is represented as a solid wall of the same height and as a result the SVF in the pixels surrounding it are significantly lowered.

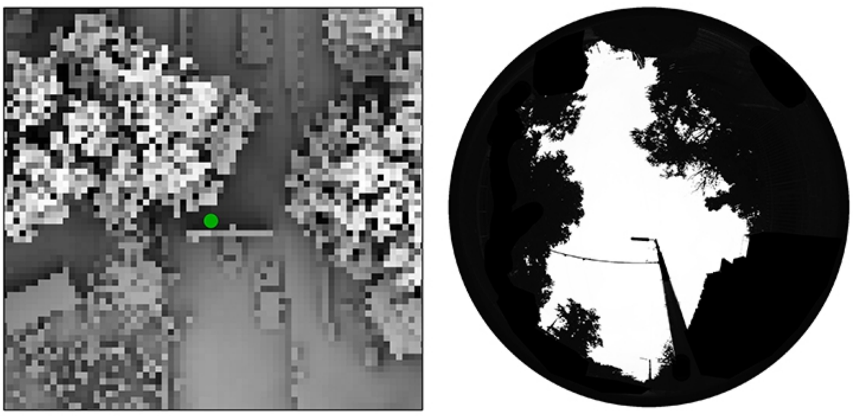

Figure 26. *SVF outlier influenced by a DSM artifact (left) and corresponding obstruction mask from fisheye photograph (right).*

As the canopy coincident points are poorly represented in both models and contribute to extreme errors, the comparison becomes clearer when they are removed from the dataset. Then it can be seen that the maps without trees significantly overestimate the measured values (fig. 27).

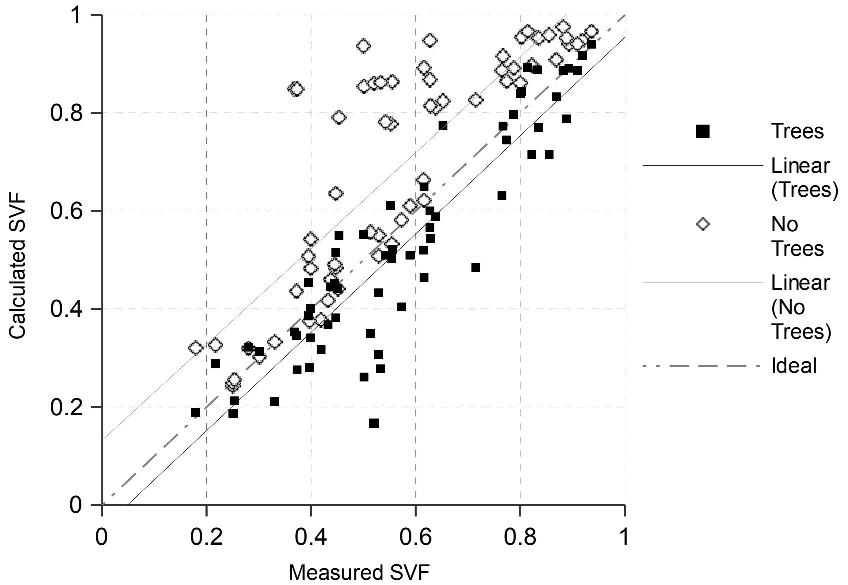

Figure 27. *Predicted SVF versus measured SVF*

While the SVF maps generated with tree canopy data underestimate the observed values, they provide a closer fit. A box plot of the residuals (see fig. 28) reveals the differences in the variation between the two estimates.

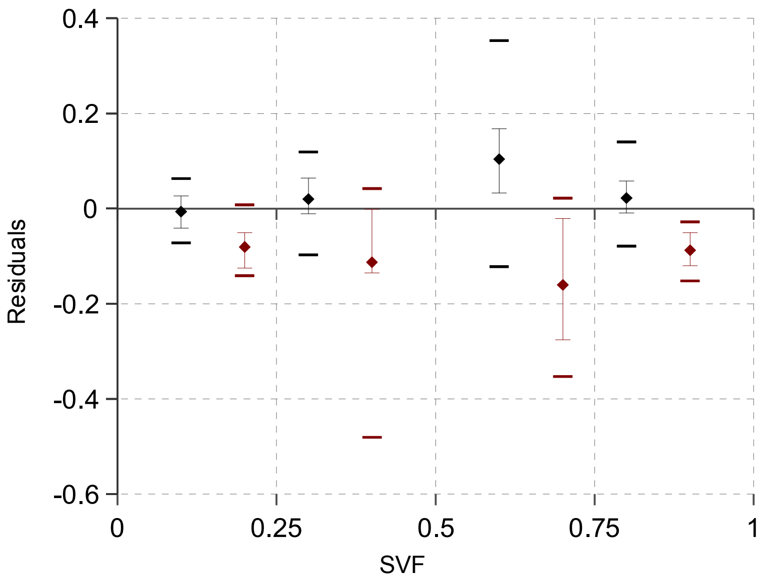

Figure 28. *Residual box plot of calculated SVF with trees (black) and without (red). Error bars show first and third quartiles, dashes represent maximum and minimum values.*

When the cumulative error distributions of the two sets are examined, it is even more clear that the continuous SVF maps generated from the DSM including trees correspond better with measured values taken during full leaf season than those generated from a DEM including only buildings (see fig. 29).

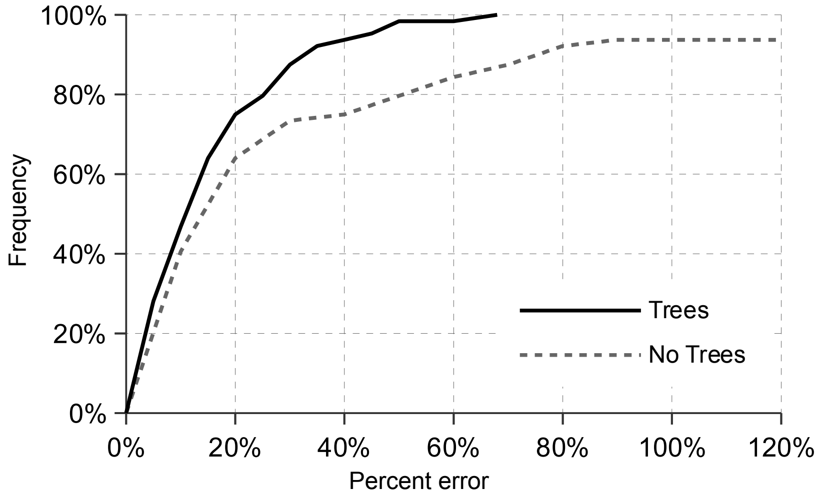

Figure 29. *Comparison of cumulative error for continuous SVF maps*

4.1.2. Sampling

As mentioned above (see section 3.3.3.), the combination of 3 land-use filters and 4 distance weighting methods lead to 12 results for each continuous SVF map. Results from the sampling methods can be seen in Table A1 in the appendix. Variation of SVF between the sampling methods in the study areas was relatively low. Most had a standard deviation at or below 0.05.

The exception to this is the Innere Stadt (IS) study area, where there is more variation ($\sigma = 0.09$). Presumably, this occurs because the weather station is located in one of the narrower street canyons. Therefore, when the SVF values are weighted by the inverse square of the distance from the station ($1/r^2$), this strongly weights the local values within the street canyon compared to the more open areas in the region (see fig. 30).

The overall low degree of variation across sampling methods indicates a certain stability in the representative value of SVF for urban areas of this size. This is further reinforced below in section 4.1.3. Relationship of SVF to UHII.

Figure 30. *SVF map with Innere Stadt weather station*

4.1.3. Relationship of SVF to UHII

As previously discussed, a variety of studies have established relationships between SVF and UHII, particularly during clear, calm nights. In this context, it was of interest to determine which of the SVF sampling methods produced values that had the strongest relationship to UHII. A simple linear regression was performed for each set of SVF values with respect to UHII values derived from the historic weather data. The coefficients of determination for all pairings can be seen in table A2.

Given the connection of SVF to nocturnal cooling, it is no surprise that the correlations where much higher during the night and practically nonexistent during the day. However, it is somewhat counterintuitive that despite the better prediction of measured values, SVF values generated with tree canopy data have a consistently lower correlation with UHII than those generated without trees. This holds true for both the summer and winter seasons, regardless of the sampling method used.

This is most likely attributable to using a single SVF value as a proxy for the obstruction of longwave radiation for both trees and buildings together. This essentially treats them as obstructions with the same properties. Yet, tree canopies behave in a different fashion to built obstructions. For instance, their temperature is likely to be lower than surrounding buildings and evapotranspiration will result in a portion of the energy exchange being converted to latent heat and thus not contributing to UHII.

Furthermore, in all cases the correlation was highest during the summer season. The strongest relationships occurred with unweighted, building-masked SVF values during summer nights (see fig. 31).

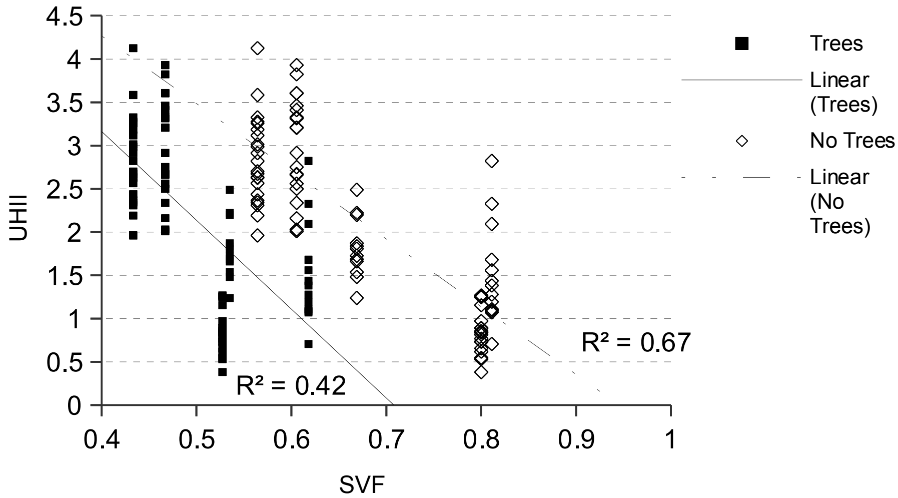

Figure 31. *Unweighted, building-masked SVF compared to UHII on summer nights*

Also note that the x-intercept of the linear regression line for the treeless SVF is significantly closer to 1. This is a better fit to the assumption being tested, namely that SVF is primary factor driving the difference in temperature between the urban and rural sites. As the rural area has a predominately unobstructed sky view, UHII should be null when SVF is 1.

4.2 Shortwave Radiation

The shortwave radiation algorithm (SRA) used in this study provides maps of the spatial distribution of incoming solar radiation at a given time (see fig. 32). The temporal and spatial resolution is only limited by that of the input data. In this study, the input data was collected at 1 minute intervals and the SRA was used to create a map to correspond with each measurement. However, an interval of only 10 minutes is recommended by (Yu, et al. 2009) for shadow calculations in urban areas. Like the SVF algorithm, the spatial resolution of the output was 0.25 m^2.

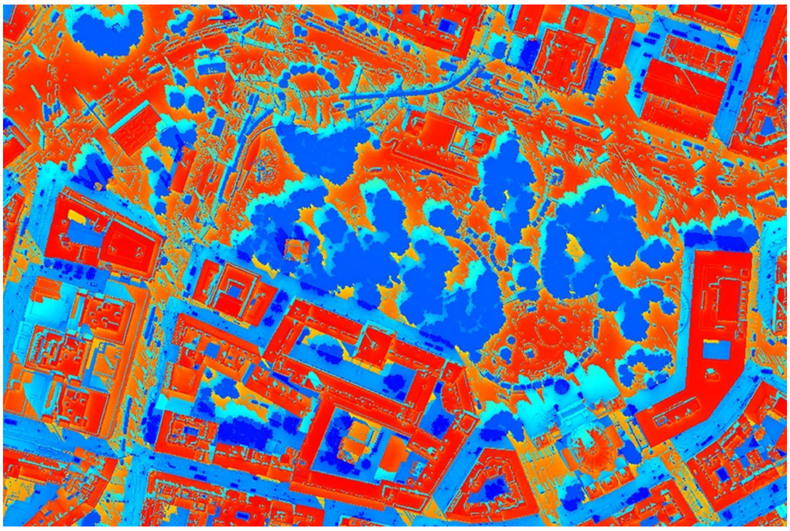

Figure 32. *Solar irradiance map. Resselpark, Vienna. 22.8.2013 11:35 AM*

4.2.1. Validation

The SOLWEIG model currently only allows for calculations at 1 hour intervals. For comparison, the values measured under tree canopies at 1 minute intervals and the corresponding values calculated by the SRA were averaged over each hour.

As described in section 3.4.2., the values measured in clear sky conditions were taken in 45 minute increments. To further complicate matters, these periods occasionally overlap 2 one-hour periods. In order to compare the SOLWEIG estimates to these asynchronous measurement periods, the mean value of the estimates from both periods is used. Whereas the 1 minute interval estimates from the SRA are simply averaged over the given period. The results from the two models can be seen in figure 33 below.

Analyzing three of the outliers (labeled in fig. 33) in greater detail reveals both key sources of error in the model and the problematic nature of validating a solar irradiance model in a environment with complex shading obstructions. As mentioned in section 2.2.2., during clear sky conditions, the direct component constitutes the largest portion of the incoming shortwave radiation. This results in significant spatial discontinuities at the boundary between areas in full sun and those shaded by trees and buildings. Locations 3 and 12 highlight how even a small uncertainty in the position of the sensor can lead to both extreme over- and underestimates (see fig. 35).

The outlier at location 24 demonstrates the improvement of the SOLWEIG model's tree representation over the simplified method used in this model (refer to section 3.4.1.). As shown in figure 36, the SOLWEIG model is able to account for the direct solar irradiance received under the tree canopy at a low sun angle, whereas the SRA severely underestimates this value.

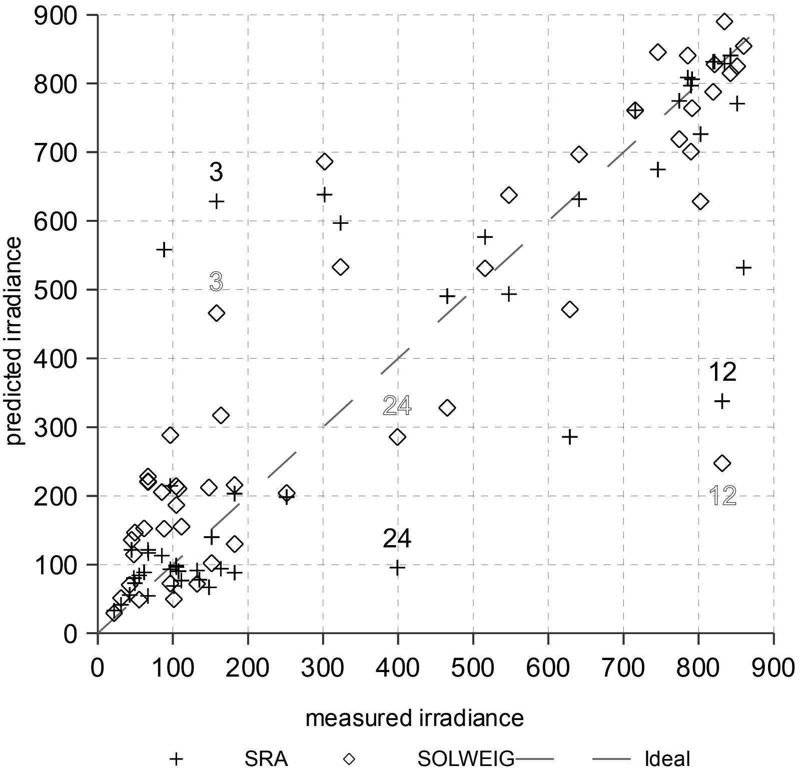

Figure 33. *Global irradiance models compared to measured values. Exemplary outliers labeled by location ID.*

Examining the cumulative frequency of the error (fig. 34) shows that despite the simplifications in the SRA model, it preforms better overall. This is likely due to the finer temporal resolution of the SRA versus the SOLWEIG model. Even averaged over an hour the 1 minute time step better captures dynamic shading conditions than a single sun position taken every half hour.

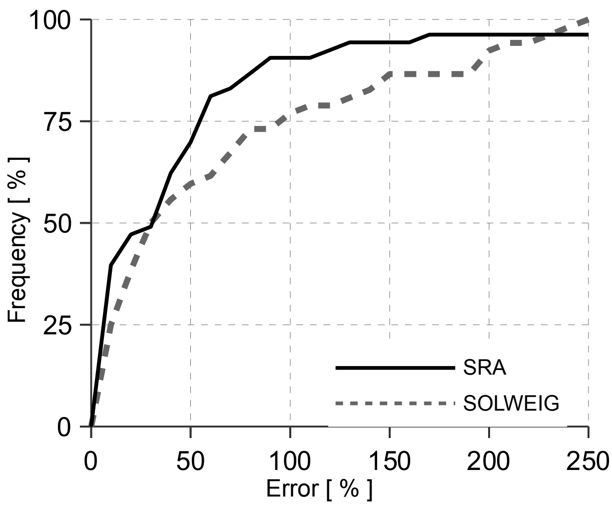

Figure 34. *Cumulative frequency of error for the SRA and SOLWEIG predictions of shortwave irradiance*

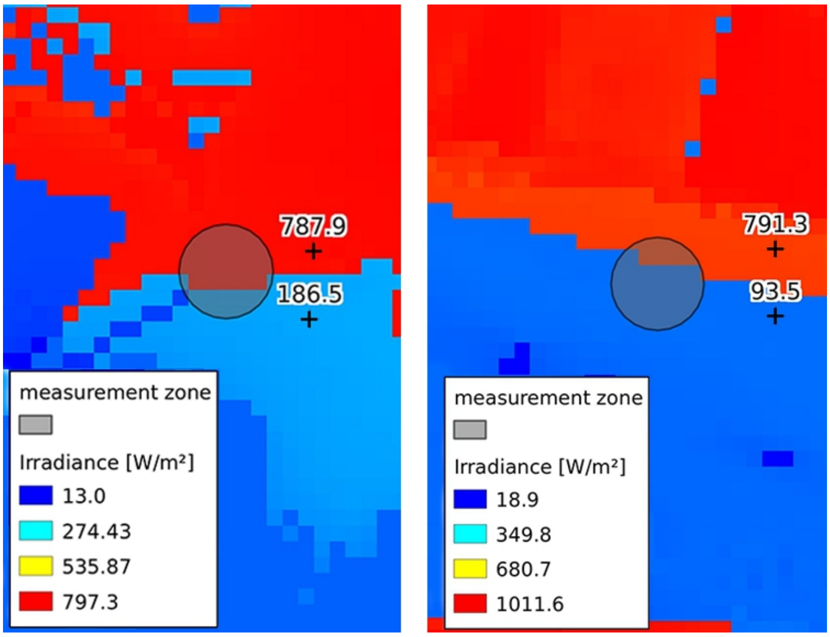

Figure 35. *Outliers – Location 3 (left) and location 12 (right)*

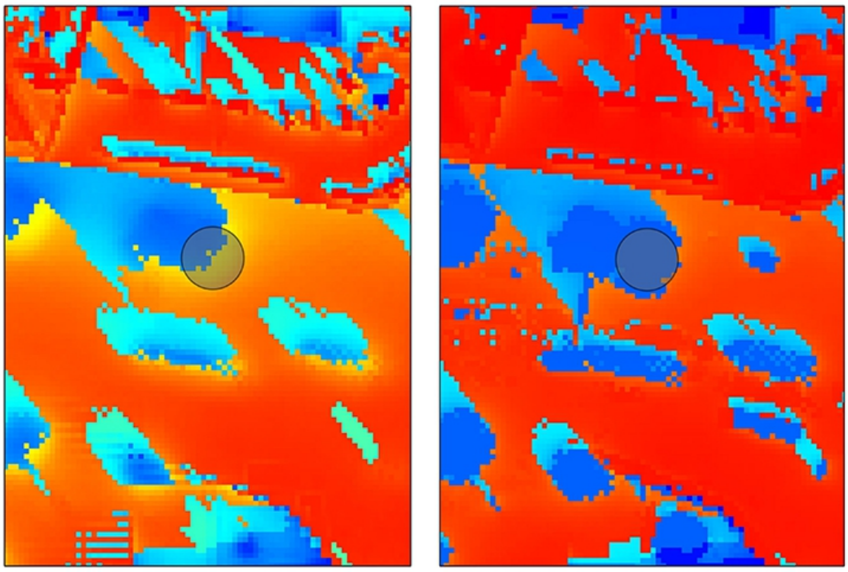

Figure 36. *Tree canopy results for the SOLWEIG model (left) and the SRA (right) at location 24.*

5 Discussion

5.1 Summary

This research was centered around the implementation of algorithmic methods for calculating continuous SVF maps and estimating the spatial distribution of global shortwave irradiance in an urban environment. In each case the role of trees and the methods for representing them were analyzed in relation to field measurements. Understanding and accurately modelling the impact of trees on the energy budget of the urban system is important in the context of the UHI phenomenon.

The SVF maps were generated from DEMs both with and without tree canopy information and the results compared with hemispherical photographic measurements of SVF. To test the relationship of SVF to UHII, a linear regression analysis was performed with 27 years of weather data categorized by season and time of day for 5 study areas in the city of Vienna, Austria.

The model for calculating shortwave irradiance was based on a simplification of the SOLWEIG model and an adaptation of the SVF algorithm. This model uses a DEM and measurements of global and diffuse irradiance from a reference weather station as input. The results were compared to the SOLWEIG model, as well as field measurements beneath tree canopies and in more open conditions.

5.2 Conclusions

5.2.1. SVF

The continuous SVF maps produced by the algorithm showed good equivalence with values measured via hemispherical photography. This was particularly true of the SVF values generated from DEMs including tree canopy information. However, these values showed a lower degree of correlation with UHII values compared to the treeless SVF values.

This seeming contradiction is most likely attributable to using a single value for SVF to represent the obstructions of both trees and built objects together. In other words, as SVF's primary relationship with UHII is the reduction in the longwave radiation exchange with the sky, using a single for both trees and buildings doesn't allow for differences between the two types of obstructions. In particular, this ignores differences in their surface temperature and evapotranspiration. This can be avoided by the used of two separate

DEMs for buildings and vegetation as shown in (Lindberg and Grimmond 2011).

In terms of expressing a relationship with UHII, these results indicate that it is better to use a SVF value calculated from a DEM without trees than to use a SVF value that combines both trees and buildings together.

Furthermore, this relationship was found to only be significant during the night. This result corresponds well with the notion that SVF is a key parameter in the determination of nocturnal cooling. The strength of the correlation decreases during the winter season and this is likely due to other climatic conditions such as higher wind speeds and less overall solar radiation absorbed during shorter days with lower sun angles.

Additionally, several distance weighting methods and land-use filters were used to calculate different areal mean values for SVF. The variation within the results was found to be rather low and use of the weighting methods provided no increase in the correlation with historic UHII values. This suggests that a study area of the size used in this study (i.e. a circular area with a radius of 350m) is already small enough to capture the essential nature of an urban area without additional weighting schemes.

However, SVF values averaged without including building areas showed a consistently higher correlation to UHII. This indicates that the mechanisms relating SVF to UHII are predominately driven by factors within the Urban Canopy Layer.

5.2.2. Shortwave Radiation Algorithm

The values derived from the SRA corresponded well with measured values, for the most part. However, the large discontinuities in irradiance values between areas of full sun and shade combined with uncertainty in the position of the measurement devices resulted in several outliers.

Furthermore, these values were compared with the SOLWEIG model on which the algorithm was based. Despite being a simplification of the SOLWEIG model the SRA showed better overall fit to measured values. This is the most likely the result of a finer temporal resolution. The values for the SRA are calculated at one minute intervals and averaged for the hour. The SOLWEIG model, on the other hand, only calculates one value using the sun's position in the middle of the one hour period.

It should be noted that in locations directly beneath tree canopies the SOLWEIG model showed much better estimates of incoming irradiance at low sun angles. This is attributable to the improved representation of trees in the SOLWEIG model using multiple DEMs to account for the trunk zone below the canopy (refer to fig. 18).

If an area average was used as a representative value for a given study area, similar to the SVF method, it is likely that this approach would be sufficient for providing a rough estimate of the amount of shortwave irradiance received across an urban area. However, as Lindberg and Grimmond (2011) point out, in cities the trunk zone is a frequently occupied and utilized area. Without the use of a more sophisticated vegetation scheme, values calculated in these areas are circumspect.

5.3 Future Work

At the end of any successful research effort there are many ways forward. However, there is one aspect, in particular, that needs to be addressed in subsequent studies. This is the low number of element pairs involved in the analysis. To quote (Unger 2009) "investigation of a sufficient number of appropriate-sized areas covering the largest part of a city or the entire city is needed to draw well-established conclusions on the studied relationship."

The availability of the historical data from the 5 weather stations in our study areas was invaluable for examining the seasonal variations (see figs. A2 and A3 in the appendix). Furthermore, having over 25 years of weather data gives an assurance that any relationship uncovered is not the product of a single seasonal anomaly. That being said, the measured temperature values at both the urban and rural reference stations are spatially fixed measurements taken as being representative for the entire study area. In the case of the SVF analysis, they were compared to area average values of SVF that, as discussed previously, are assumed to be static over time.

In the vein of (Unger 2009; Blankenstein and Kuttler 2004), systematic data gathering across a grid of equally sized cells using mobile measurement transects would provide more insight into the spatial distribution of the UHI phenomenon. Additionally, future measurements should also directly record longwave radiation flux.

Even though the historic data lacks measurements of longwave radiation flux, several parameterizations of sky emissivity exist that use more common climatic measurements taken by these weather stations. Using these methods in combination with the SVF measures would allow for estimations of the longwave radiation flux that would vary temporally and may reveal a stronger relationship to overnight UHII. Furthermore, the United States' Geological Survey (USGS) has freely available historic Landsat satellite imagery with spectral bands in the infrared spectrum. These could be used to determine the spatial distribution of surface temperature, albeit at relatively large time steps and spatial resolution. Additionally, as radiative cooling is particularly dominate during calm nights, filtering the historic data based on wind speed would better isolate the effect.

According to (Robinson 2011), the use of the Perez anisotropic sky model, which is a background-circumsolar-horizon model, predicts differences of 15-20% in the annual diffuse radiation over the isotropic model depending on orientation of receiving surface. An anisotropic sky model could be integrated with the SVF algorithm presented in this paper by encoding not only the intersection with the measurement plane (e.g. ground) from a particular sky vector, but also the origin of that vector in a discretized sky hemisphere.

Following the analysis of the outliers in the shortwave radiation model and the comparison to the SOLWEIG results, it is clear that that an improved representation of trees in the DEMs is necessary. This is particularly true at low sun angles. Similar to the SOLWEIG model it should be possible to automatically estimate the under canopy height using some fixed proportion of the canopy height. More interesting, however, would be pairing this with the city of Vienna's extensive GIS-based tree registry to distinguish tree shapes based on species or simply between coniferous and deciduous. This improvement would help with both shortwave and longwave calculations.

Another improvement in future efforts would be to investigate methods for automatically cleaning the DEM of ghosts and artifacts from the lidar scan. Again the Vienna tree registry could be of use here by applying it to filter tree pixels from non-tree pixels. Also using a threshold for the minimum size of a group of canopy pixels should eliminate many of the small artifacts.

6 References

6.1 Literature

Akbari, H., Pomerantz, M., & Taha, H. 2001. Cool surfaces and shade trees to reduce energy use and improve air quality in urban areas. *Solar energy*, 70(3), 295-310.

Akbari, H. 2005. Energy Saving Potentials and Air Quality Benefits of Urban Heat Island Mitigation, Lawrence Berkeley National Laboratory, Berkeley, CA.

Attwell, K. 2000. Urban land resources and urban planting—case studies from Denmark. *Landscape and Urban Planning*, 52(2), 145-163.

Bärring, L., Mattsson, J. O., & Lindqvist, S. 1985. Canyon geometry, street temperatures and urban heat island in Malmö, Sweden. *Journal of Climatology*, 5(4), 433-444.

Blankenstein, S., & Kuttler, W. 2004. Impact of street geometry on downward longwave radiation and air temperature in an urban environment. *Meteorologische Zeitschrift*, 13(5), 373-379.

Block, A. H., Livesley, S. J., & Williams, N. S. 2012. Responding to the Urban Heat Island: A Review of the Potential of Green Infrastructure.
Retrieved from http://www.vcccar.org.au/publications

Brown, M. J., Grimmond, S., & Ratti, C. 2001. Comparison of methodologies for computing sky view factor in urban environments. In *International Society of Environmental Hydraulics Conference, Tempe, AZ.*

Bruse, M. 2004. *ENVI-met 3.0: Updated model overview*. University of Bochum. Available at: www.envi-met.com

Chen, L., Ng, E., An, X., Ren, C., Lee, M., Wang, U., & He, Z. 2012. Sky view factor analysis of street canyons and its implications for daytime intra‐urban air temperature differentials in high‐rise, high‐density urban areas of Hong Kong: a GIS‐based simulation approach. *International Journal of Climatology, 32*(1), 121-136.

Delta-T. 2013. *SPN1 Sunshine Pyranometer - Solar Radiation Measurement.* Retrieved from
http://www.delta-t.co.uk/product-display.asp?
id=SPN1%20Product&div=Meteorology%20and%20Solar

Ennos, R. 2012. Quantifying the cooling benefits of urban trees. In Johnston, M. and Percival, G. eds. *Trees, people and the built environment. Proceedings of the Urban Trees Research*

Conference 13–14 April 2011. (pp. 113-118) Edinburgh: Forestry Commission, Silvan House.

Essery, R., Pomeroy, J., Ellis, C., & Link, T. 2008. Modelling longwave radiation to snow beneath forest canopies using hemispherical photography or linear regression. *Hydrological Processes*, 22(15), 2788-2800.

Gál, T.,, Lindberg, F., Unger, J. 2009. Computing continuous sky view factors using 3D urban raster and vector databases: comparison and application to urban climate. *Theoretical and Applied Climatology*, 95 (1-2), 111–123.

Gartland, L. 2011. *Heat islands: understanding and mitigating heat in urban areas.* London: Routledge.

Hardy, J. P., Melloh, R., Koenig, G., Marks, D., Winstral, A., Pomeroy, J. W., & Link, T. 2004. Solar radiation transmission through conifer canopies. *Agricultural and Forest Meteorology*, 126(3), 257-270.

Harlan, S L., Ruddell, D.M. 2011. Climate change and health in cities: impacts of heat and air pollution and potential co-benefits from mitigation and adaptation. *Current Opinion in Environmental Sustainability*, 3(3), 126-134.

Holmer, B., Postgård, U. and Eriksson, M. 2001. Sky view factors in forest canopies calculated with IDRISI. *Theoretical and Applied Climatology,* 68, 33-40.

Huttner, S. 2012. *Further development and application of the 3D microclimate simulation ENVI-met* (Doctoral dissertation, Mainz, Univ., Diss., 2012).

Johnson, G.T., & Watson, I. D. 1984. The determination of view-factors in urban canyons. *Journal of Climate and Applied Meteorology*, 23, 329-335.

Jonckheere, I., Fleck, S., Nackaerts, K., Muys, B., Coppin, P., Weiss, M., & Baret, F. 2004. Review of methods for in situ leaf area index determination: Part I. Theories, sensors and hemispherical photography. *Agricultural and forest meteorology*, 121(1), 19-35.

Landsberg, H. E. 1981. *The urban climate* (Vol. 28). New York: Academic press.

Lindberg F. 2005. Towards the use of local governmental 3-D data within urban climatology studies. *Mapping and Image Science,* 2, 32–37.

Lindberg F. 2007. Modelling the urban climate using a local governmental geo-database. *Meteorological Applications,* 14, 263–273.

Lindberg, F., Holmer, B., & Thorsson, S. 2008. SOLWEIG 1.0–Modelling spatial variations of 3D radiant fluxes and mean radiant temperature in complex urban settings. *International Journal of Biometeorology*, 52(7), 697-713.

Lindberg, F., & Grimmond, C.S.B. 2011. The influence of vegetation and building morphology on shadow patterns and mean radiant temperatures in urban areas: model development and evaluation. *Theoretical and applied climatology*, 105(3-4), 311-323.

Matzarakis, A., Rutz, F., & Mayer, H. 2010. Modelling radiation fluxes in simple and complex environments: basics of the RayMan model. *International Journal of Biometeorology*, 54(2), 131-139.

Nowak, D. J. 1996. Notes: estimating leaf area and leaf biomass of open-grown deciduous urban trees. *Forest Science*, 42(4), 504-507.

Nunez, M., & Oke, T.R. 1976. Long-wave radiative flux divergence and nocturnal cooling of the urban atmosphere. *Boundary-Layer Meteorology*, 10(2), 121-135.

Nunez, M., Eliasson, I., & Lindgren, J. 2000. Spatial variations of incoming longwave radiation in Göteborg, Sweden. *Theoretical and Applied Climatology*, 67(3-4), 181-192.

Oke, T.R. 1981. Canyon geometry and the nocturnal urban heat island: comparison of scale model and field observations. *Journal of Climatology,* 1, 237–254.

Oke, T.R. 1987. *Boundary Layer Climates, 2nd ed.* London: Routledge.

Ong, B. L. 2003. Green plot ratio: an ecological measure for architecture and urban planning. *Landscape and Urban Planning*, 63(4), 197-211.

QGIS Development Team. 2013. QGIS Geographic Information System. Open Source Geospatial Foundation Project. Available at: http://qgis.osgeo.org

Richens, P. 1997. Image processing for urban scale environmental modelling. In *Proceedings of the 5th International IBPSA Conference: Building Simulation 97*, Prague.

Robinson, D. (Ed.). 2011. *Computer Modelling for Sustainable Urban Design: Physical Principles, Methods and Applications*. London: Routledge.

Samaali, M., Courault, D., Bruse, M., Olioso, A., & Occelli, R. 2007. Analysis of a 3D boundary layer model at local scale: Validation on soybean surface radiative measurements. *Atmospheric research*, 85(2), 183-198.

Shashua-Bar, L., & Hoffman, M. E. 2002. The Green CTTC model for predicting the air temperature in small urban wooded sites. *Building and Environment*, 37(12), 1279-1288.

Stewart, I. D., & Oke, T. R. 2012. Local climate zones for urban temperature studies. *Bulletin of the American Meteorological Society*, 93(12), 1879-1900.

Steyn, D.G. 1980. The calculation of view factors from fisheye‐lens photographs: Research note. *Atmosphere-Ocean*, 18(3), 254-258.

Svensson, M. K. 2004. Sky view factor analysis–implications for urban air temperature differences. *Meteorological Applications*, 11(03), 201-211.

UHI. 2013. The UHI Project. Retrieved from http://www.eu-uhi.eu/

Unger, J. 2004. Intra-urban relationship between surface geometry and urban heat island: review and new approach. *Climate Research*, 27(3), 253-264.

Unger, J. 2009. Connection between urban heat island and sky view factor approximated by a software tool on a 3D urban database. *International Journal of Environment and Pollution*, 36(1), 59-80.

United Nations. Department of Economic and Social Affairs. Population Division. 2012. *World urbanization prospects: the 2011 revision.* UN.

USDA Forest Service. 2012. i-Tree: Tools for Assessing and Managing Community Forests. Available at: www.itreetools.org

Voogt, J. A. 2002. Urban heat island. In Munn, T. (Ed.), *Encyclopedia of Global Environmental Change, Vol. 3* (660-666). Chichester: Wiley.

Wood, J. 2012. *Using the DNI_Demo spreadsheet.* Retrieved from http://www.delta-t.co.uk/product-support-material.asp

Yu, B., Liu, H., Wu, J., & Lin, W. M. 2009. Investigating impacts of urban morphology on spatio-temporal variations of solar radiation with airborne LIDAR data and a solar flux model: a case study of downtown Houston. I*nternational Journal of Remote Sensing*, 30(17), 4359-4385.

6.2 Tables

6.3 Figures

6.4 Equations

Appendix

Table 5. *Representative values of SVF by sampling method*

	Trees															No Trees														
	Building Mask				Streets				Whole Area							Building Mask				Streets				Whole Area						
Location	none	$1/r^2$	$1/r$	$1/\sqrt{r}$	none	$1/r^2$	$1/r$	$1/\sqrt{r}$	none	$1/r^2$	$1/r$	$1/\sqrt{r}$	Mean	Range	Stdev.	none	$1/r^2$	$1/r$	$1/\sqrt{r}$	none	$1/r^2$	$1/r$	$1/\sqrt{r}$	none	$1/r^2$	$1/r$	$1/\sqrt{r}$	Mean	Range	Stdev.
DF	0.62	0.61	0.62	0.62	0.69	0.71	0.70	0.69	0.66	0.67	0.67	0.67	0.66	0.09	0.03	0.81	0.74	0.80	0.81	0.88	0.91	0.89	0.89	0.82	0.78	0.81	0.82	0.83	0.16	0.05
GDZ	0.53	0.51	0.56	0.55	0.54	0.54	0.55	0.55	0.61	0.55	0.62	0.61	0.56	0.11	0.03	0.67	0.67	0.70	0.69	0.67	0.70	0.70	0.68	0.69	0.66	0.71	0.70	0.69	0.06	0.02
HW	0.53	0.60	0.53	0.53	0.46	0.46	0.46	0.46	0.55	0.61	0.55	0.55	0.52	0.15	0.05	0.80	0.84	0.80	0.8	0.81	0.76	0.79	0.80	0.79	0.83	0.79	0.79	0.80	0.08	0.02
AKH	0.47	0.50	0.49	0.48	0.45	0.47	0.46	0.46	0.59	0.64	0.61	0.60	0.52	0.19	0.07	0.61	0.65	0.63	0.62	0.60	0.67	0.64	0.62	0.67	0.66	0.67	0.67	0.64	0.07	0.02
IS	0.43	0.30	0.40	0.42	0.43	0.29	0.40	0.42	0.55	0.40	0.53	0.54	0.43	0.26	0.08	0.56	0.35	0.51	0.55	0.54	0.34	0.49	0.53	0.63	0.44	0.59	0.61	0.51	0.29	0.09

Table 6. *Coefficients of determination for the relationship between UHII and SVF*

	Trees												No Trees											
	Building Mask				Streets				Whole Area				Building Mask				Streets				Whole Area			
	none	$1/r^2$	$1/r$	$1/\sqrt{r}$	none	$1/r^2$	$1/r$	$1/\sqrt{r}$	none	$1/r^2$	$1/r$	$1/\sqrt{r}$	none	$1/r^2$	$1/r$	$1/\sqrt{r}$	none	$1/r^2$	$1/r$	$1/\sqrt{r}$	none	$1/r^2$	$1/r$	$1/\sqrt{r}$
Winter Nights	0.35	0.25	0.25	0.30	0.18	0.15	0.16	0.17	-	0.07	-	-	0.50	0.25	0.40	0.46	0.46	0.21	0.36	0.42	0.47	0.30	0.41	0.45
Summer Nights	0.42	0.42	0.35	0.38	0.15	0.19	0.16	0.15	-	0.14	-	-	**0.66**	0.47	0.60	0.64	0.58	0.33	0.49	0.55	0.60	0.50	0.58	0.60
Winter Days	0.08	0.05	0.05	0.06	-	-	-	-	-	-	-	-	0.14	0.07	0.11	0.13	0.12	0.04	0.08	0.10	0.12	0.08	0.11	0.12
Summer Days	-	-	-	-	0.10	-	0.06	0.08	0.06	-	-	-	-	0.05	-	-	-	-	-	-	-	-	-	-

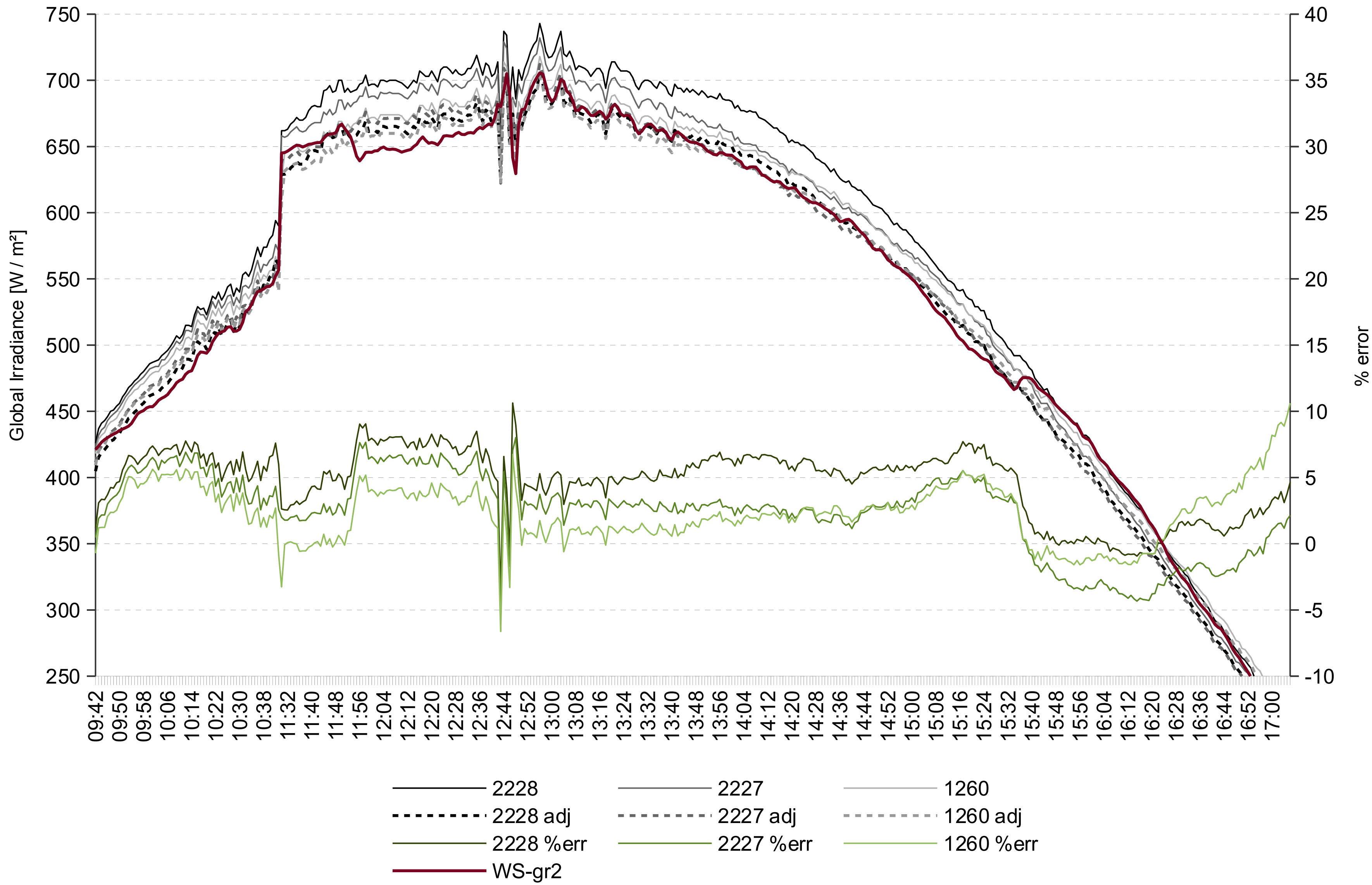

Figure A1. *Calibration results for Schenk pyranometers*

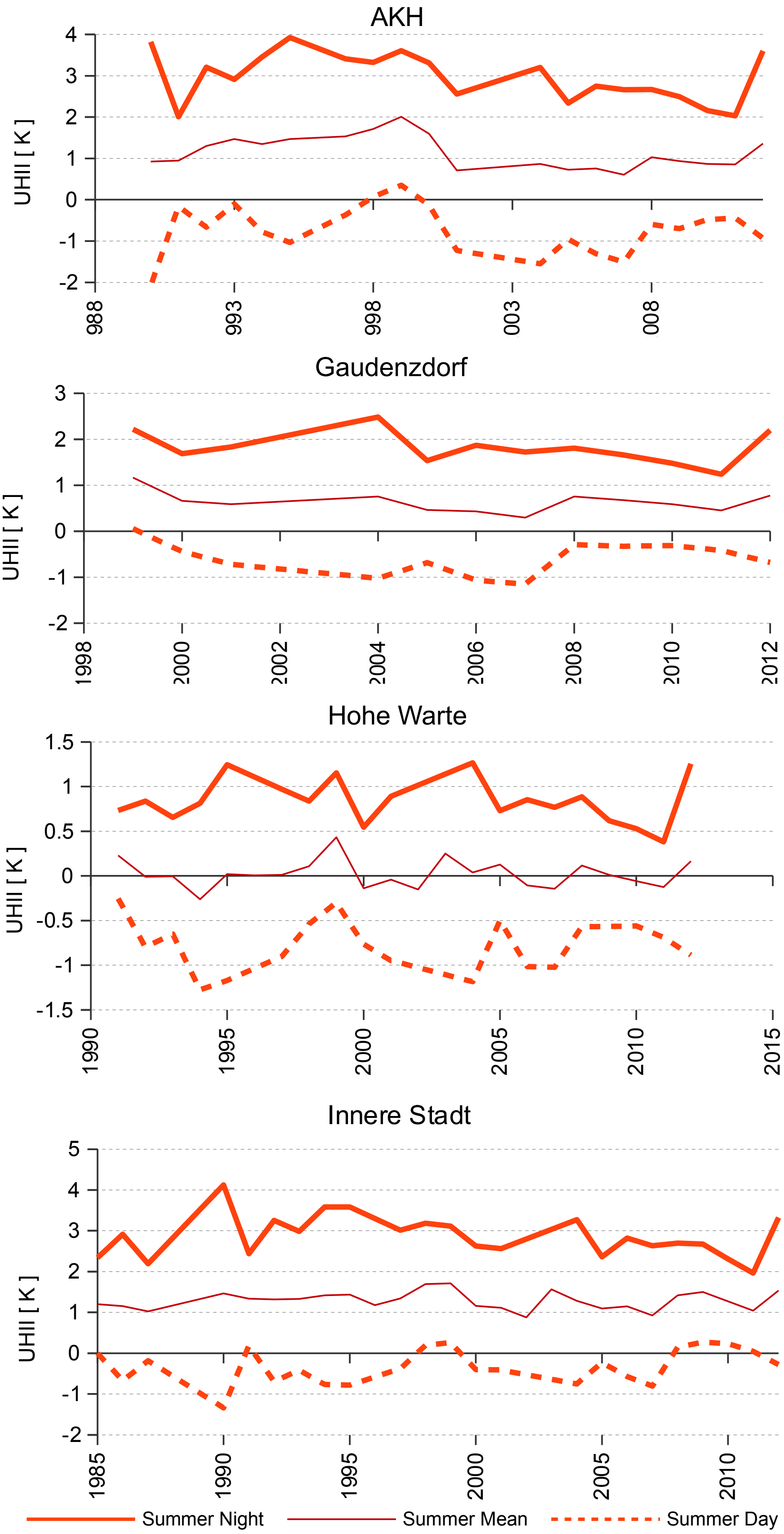

Figure A2. *Summer season average UHII values*

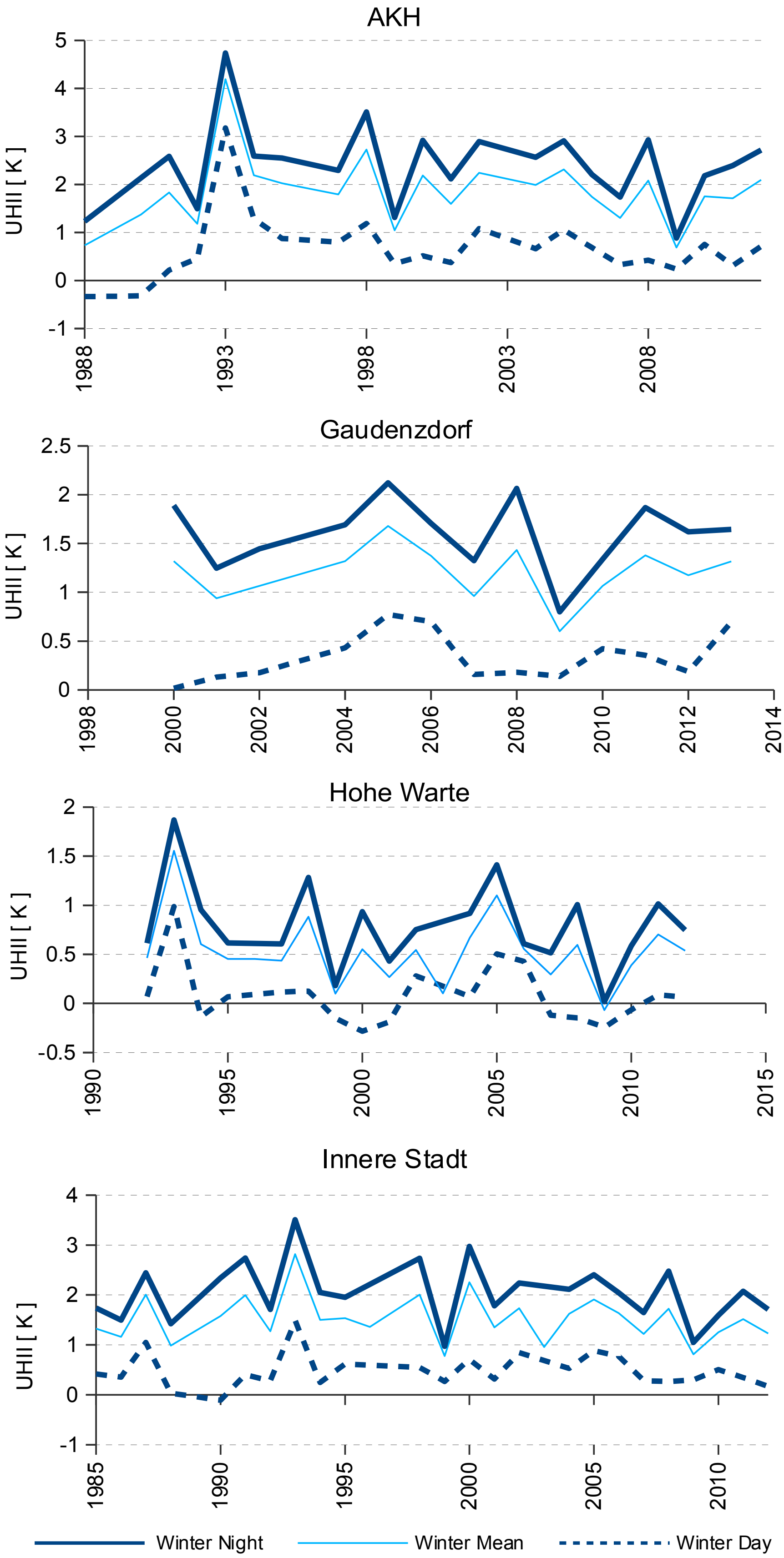

Figure A3. *Winter season average UHII values by study area*